Striatal activity topographically reflects cortical activity

Andrew J Peters[1*], Julie MJ Fabre[2], Nicholas A Steinmetz[1,2,3], Kenneth D Harris[2], and Matteo Carandini[1]

[1]Institute of Ophthalmology, University College London, London, UK
[2]Institute of Neurology, University College London, London, UK
[3]Present address: Department of Biological Structure, University of Washington, Seattle, WA
*e-mail: peters.andrew.j@gmail.com

The dorsal striatum is associated with multiple sensory[1–3], motor[4], and cognitive[5,6] roles. This variety of roles is also characteristic of the cortex, which projects to the striatum topographically[7,8] to regulate behavior[9–11]. Yet, spiking activity has been reported to have markedly different relation to sensorimotor events in the cortex and striatum [12–15], raising the question of how activity is transformed between the two structures. Here we reveal a precise, causal, and topographic relationship between spatiotemporal activity in the cortex and the dorsal striatum, and show that cortical activity predicts striatal activity both within and outside sensorimotor behavior. We simultaneously imaged the entire dorsal cortex and recorded through the width of the dorsal striatum in mice performing a visually-guided task. The behavioral correlates of striatal activity followed a mediolateral gradient from visual to movement to licking responses. The summed activity in each part of striatum closely and specifically mirrored activity in topographically associated cortical regions. Inactivation of the visual cortex abolished striatal responses to visual stimuli, indicating that cortex plays a causal role in driving these striatal responses. Individual medium spiny neurons (MSNs) and fast-spiking interneurons (FSIs) in the striatum fired at specific times relative to sensorimotor events, and together they matched the activity of topographically associated cortical regions. In contrast, tonically active neurons (TANs) responded stereotypically to sensory and reward events and differed from cortical activity. Striatal visual responses occurred inside or outside of task performance, and increased with training[16] particularly in MSNs and TANs without corresponding changes in cortical activity. Striatal activity therefore reflects a consistent and causal topographic mapping of cortical activity.

Cortical neurons provide a major synaptic input to the dorsal striatum[17,18], but the degree to which they control striatal activity is unclear. With few exceptions[19,20] electrophysiological recordings have suggested marked differences in sensory and behavioral correlates between striatal and cortical neurons[12–15], and between striatal cell types[13,21–23]. Accordingly, striatum receives inputs from multiple other structures beyond the cortex, including the thalamus[24,25] and other nuclei in the basal ganglia[26], which can target specific striatal cell types[27]. Furthermore, local striatal circuitry could transform cortical inputs[28], for example to extract specific sensory or behavioral features[16,20,29–36].

Nevertheless, the possibility remains that cortical and striatal activity are similar, but that this similarity is only apparent in topographically matched regions. Corticostriatal inputs are topographically ordered[7,8,37] and indeed cortical and striatal fMRI signals measured in humans at rest are topographically correlated[38]. Recording neural activity concurrently from matched regions would be difficult with methods that sample only local neural populations in each structure. To resolve this difficulty, we thus sought a more comprehensive approach: we imaged activity across wide areas of the cortex and

simultaneously recorded the spikes of hundreds of neurons along the width of the striatum while mice performed a sensorimotor task.

Progression of task-related activity

We trained mice in a visual task[39] (**Fig. 1a**). After an enforced 500 ms quiescent period, a grating of variable contrast appeared on the left or right. The stimulus remained fixed for 500 ms, then an auditory Go cue signaled that the stimulus position became yoked to a steering wheel and could be brought to the center to elicit a water reward (**Fig. 1a, Extended Data Fig. 1a**). The correct response to a stimulus on the right (contralateral to the striatal recordings), was to turn the wheel counterclockwise, moving the stimulus from right to center. We refer to such movements as "contralaterally-orienting". Mice performed the task well, approaching 100% accuracy for high-contrast stimuli (**Extended Data Fig. 1b**). They typically began turning the wheel before the Go cue, especially at the beginning of a session (**Extended Data Fig. 1c-d**).

While mice performed this task, we recorded activity simultaneously across the dorsal cortex and along a trajectory spanning the width of the dorsal striatum (**Fig. 1b, c**). To record cortical activity, we used widefield calcium imaging of excitatory neurons (CaMK2a-tTa;tetO-GC6s transgenic mice; Ref. [40]), aligning the images across sessions using vasculature and across mice using retinotopic maps (**Extended Data Fig. 2**). At the same time, we recorded striatal activity with a Neuropixels probe[41] inserted along the width of the striatum in a diagonal mediolateral trajectory (n = 77 sessions across 15 mice, **Fig. 1c**). This trajectory was standardized across sessions, yielding consistent electrophysiological landmarks that marked the borders of the striatum (**Extended Data Fig. 3**).

Though the imaging was focused on the surface of the cortex, it reflected spiking activity in deep layers (**Extended Data Fig. 4**). In 3 mice we inserted a second Neuropixels probe in the visual cortex (n = 10 sessions), and determined a deconvolution kernel that optimally predicted cortical spiking from widefield activity (**Extended Data Fig. 4a-b**, fraction cross-validated explained variance 0.22 ± 0.03 mean ± s.e.m. across sessions, no difference across task or passive contexts: signed-rank test p = 0.19). The widefield signal correlated best with spiking in deep layers (**Extended Data Fig. 4c-d**), possibly because neurons there have high firing rates[42] and superficial apical dendrites[43] that drive strong fluorescence in layer 1 (Ref. [44]).

The cortex and the striatum both displayed a progression of task-related activity related to visual stimuli, movement, and licking of reward (**Fig. 1d-e**). Following the visual stimulus, cortical activity was strongest in visual (VIS) and medial secondary motor (MOs) regions, with visual cortex exhibiting a strong contralateral bias. At the time of movement, cortical activity spread to retrosplenial (RSP) and limb somatomotor (SSp-ll, SSp-ul, posterior MOp) regions, and at reward licking there was activity in the frontolateral orofacial somatomotor regions (SSp-m, MOp, lateral MOs) (**Fig. 1d**). Echoing this flow of activity, multiunit activity in the striatum progressed topographically along the mediolateral axis from visual stimulus to movement to licking (**Fig. 1e**).

Cortical and striatal topography

Correlations of striatal spikes at each depth with cortical activity revealed an orderly progression of topographic cortical maps (**Fig. 2a-e**). We computed the average cortical widefield fluorescence triggered on multiunit spiking at a succession of striatal locations from medial to lateral, obtaining maps with a steady topographic progression (**Fig. 2a**). Spike-triggered averaging, however, reflects not only the interactions between signals but also the autocorrelations within the signals. The latter are prominent during the task, as sensorimotor events often overlap with one another. To correct for these autocorrelations, we estimated spatial kernels that predict striatal spiking from cortical fluorescence.

These kernels revealed a precise cortical map for each striatal depth (**Fig. 2b**). These maps demonstrate that striatal regions along a mediolateral progression are associated with a progression of well-defined cortical regions from posterior, to frontomedial, to frontolateral (**Fig. 2c**). This progression appeared continuous, without sharp borders along the striatum. Nonetheless, for further analysis we grouped striatal locations into three domains: dorsomedial, dorsocentral, and dorsolateral striatum (DMS, DCS, and DLS, **Fig. 2d,e**), using cortical correlations to identify striatal regions without relying on estimated coordinates. This allowed us to align and pool striatal activity across sessions despite variations in probe location, pinpointing the recorded striatal location functionally.

The cortical map associated with each domain was invariant to behavior and consistent with anatomical projections (**Fig. 2f-h**). The cortical maps predicting activity of DMS, DCS, and DLS during task performance were focused on visual area AM (VISam), on frontomedial secondary motor cortex (MOs), and on frontolateral orofacial somatomotor cortex (SSp-m, MOp), respectively (**Fig. 2f**). Similar maps were obtained from activity measured while mice passively viewed retinotopic mapping stimuli (**Fig. 2g**). These results suggest a constant influence of cortex on striatum, independent of whether the animals are performing the task. Indeed, these functional cortical maps resembled patterns of corticostriatal projections reported by the Allen Mouse Brain Connectivity Atlas[37] (**Fig. 2h**), suggesting that the primary determinant of the functional corticostriatal relationship lies in fixed anatomical connectivity.

Striatal activity bore a stereotyped spatiotemporal relationship to activity in cortex (**Fig. 2i-j**). To measure the temporal relationship, we added a temporal dimension to our cortical kernels, incorporating a -100 to +100 ms lag between cortical and striatal activity. The resulting spatiotemporal patterns identified a single cortical pattern which was weighted stronger for time points where cortical activity led striatal activity (**Fig. 2i**, spatiotemporally summed cortical weights leading > lagging striatum, signed-rank test $p < 0.01$). The optimal spatiotemporal filters were unique for each domain but common across sessions and behavioral context, indicating a fundamental relationship in activity between the cortex and striatum (**Fig. 2j**, kernel correlation across contexts within session > across domains within session, signed-rank test $p < 0.01$, kernel correlation across contexts within session = across session within context, signed-rank test $p > 0.05$).

Striatal activity correlated best with deep cortical layers, with a short delay between cortical and striatal spikes consistent with monosynaptic connectivity (**Extended Data Fig. 4**). We considered data from the 3 mice where we performed widefield imaging together with one probe in the striatum and a second probe in VISam, shown above to be associated with the dorsomedial striatum (n = 10 sessions). Activity in DMS best correlated with spiking rates in VISam's deep layers (**Extended Data Fig. 4c-e**), consistent with the laminar position of corticostriatal neurons[45]. As both cortical fluorescence and firing rate in DMS were correlated to deep cortical spiking (correlation by depth not different between fluorescence and DMS spiking, correlation $r = 0.57 \pm 0.14$ mean ± s.e.m. across sessions, compared to randomly circular-shifted distribution $p < 0.01$), this suggests that the relationship between widefield cortical imaging and striatal firing rate stems from activity of corticostriatal neurons in deep cortical layers. Consistent with this hypothesis, spiking activity in the deep layers of VISam led spiking in DMS by ~3 ms, similar to previous measurements of corticostriatal lag[15] (**Extended Data Fig. 4e**).

Striatum and cortex share task responses

We next asked whether the orderly spatiotemporal maps relating cortical regions to striatal domains would be sufficient to predict the sensorimotor activity of the striatum during the task.

Firing rates in the three striatal domains were associated with three task events: contralateral stimuli (especially in DMS), contralaterally-orienting movements (especially in DCS), and reward licking (especially in DLS) (**Fig. 3a-c**). Ipsilateral stimuli did not evoke activity, while ipsilateral movements

elicited activity with similar time courses but lower amplitude than contralateral ones (**Fig 3a, Extended Data Fig. 5a**). The magnitude of visual responses observed in DMS depended on stimulus contrast but not on the animal's upcoming choice, indicating that they reflect sensory responses rather than action plans (**Extended Data Fig. 6**, 2-way ANOVA on stimulus and choice, interaction effect: DMS $p > 0.05$). To isolate the striatal correlates of individual task events, we fit striatal spiking activity as a sum of event kernels triggered on the times of stimuli of each contrast, movements in either direction, the auditory Go cue, and rewarded and unrewarded outcomes. These event kernels highlighted strong contrast-dependent contralateral stimulus responses in DMS, contralaterally-biased movement responses in DCS, and reward licking responses in DLS (**Fig. 3b**). The auditory Go cue elicited activity in parietal cortex and in DMS only in the rare instances where mice had not already begun turning the wheel (**Extended Data Fig. 7**). Together, these event kernels were sufficient to predict trial-by-trial activity observed in the striatum (**Fig. 3c, Extended Data Fig. 5b**, cross-validated $R^2 = 0.12 \pm 0.01$ in DMS, 0.35 ± 0.02 in DCS, and 0.45 ± 0.02 in DLS, mean ± s.e.m. across sessions).

Remarkably, firing rates in the three striatal domains could be predicted equally well from activity in cortex, despite no explicit inclusion of task events (**Fig. 3d-f**). For each trial, we predicted the firing rate in each striatal domain by applying the domain's unique spatiotemporal kernel to the measured cortical activity (**Fig. 3d**). This predicted firing rate was strikingly similar to the measured firing rate (**Fig. 3a,d,e**), and cortical activity predicted striatal multi-unit activity as well as or better than predictions from task events (**Fig. 3f**, cross-validated $R^2 = 0.17 \pm 0.02$ in DMS, 0.33 ± 0.03 in DCS, and 0.44 ± 0.02 in DLS, mean ± s.e.m. across sessions, $R^2_{cortex} >= R^2_{task}$, signed-rank test, $p < 0.001$ in DMS, $p > 0.05$ in DCS and DLS). This predictability occurred because the sensorimotor correlates of striatal activity were essentially identical to those of the topographically associated cortical regions, which were predicted from task events to a similar degree (**Extended Data Fig. 8**). Prediction of striatal firing from cortical activity depended on including each domain's associated cortical regions, and was superior to predictions made from other striatal domains (**Extended Data Fig. 9**). Together, these results suggest that sensorimotor responses in the striatum largely reflect activity in topographically associated cortical regions.

Striatal activity not only reflected sensorimotor responses in the cortex during behavior, but also mirrored cortical activity while mice were passive and not engaged in the task (**Extended Data Fig. 10**). When mice were passively viewing retinotopic mapping stimuli, their cortical activity predicted striatal firing rates to a similar degree as during task performance. In DMS the cortex explained slightly more variance in the passive condition than during the task (**Extended Data Fig. 10a**, signed-rank test, $p < 0.01$), likely resulting from the large oscillating, synchronous activity in the visual cortex of passive mice [46,47] which was shared with DMS (**Extended Data Fig. 10b-c**). Conversely, in DCS and DLS the cortex explained slightly less variance in the passive condition than during the task (**Extended Data Fig. 10a**, signed-rank test, $p < 0.01$ for both domains), likely reflecting decreased variance in DCS and DLS activity in the passive context (**Extended Data Fig. 10b-c**, signed-rank test, $p < 0.01$), as expected from the greatly decreased body movements.

The close match between cortical and striatal activity suggested that the striatum inherits its task responses from the cortex, and this hypothesis was confirmed by inactivation experiments (**Fig. 3g**, **Extended Data Fig. 11**). Six of the mice performed the task and passively viewed stimuli before and after inactivation of VISam with topical muscimol, while we performed widefield imaging and recorded cortical and striatal activity with a Neuropixels probe in the same hemisphere as cortical inactivation ($n = 22$ sessions across 6 mice). Cortical muscimol application effectively silenced spiking in all layers of cortex (**Extended Data Fig. 11a**) and strongly reduced visual cortical widefield responses (**Extended Data Fig. 11b**). The average firing rate in the striatum slightly increased after cortical muscimol application (**Extended Data Fig. 11c**, striatal firing rate before muscimol < after muscimol, signed-rank test $p < 0.05$

178 in all three regions), but visual responses in the dorsomedial striatum were reduced (**Fig. 3g**)
179 proportionally to the reduction in the visual cortex (**Extended Data Fig. 11d**, muscimol-induced change
180 in VISam and DMS correlation, $r = 0.48$, $p < 0.05$). Consistent with previous findings with optogenetic
181 inactivation of visual cortex[39], muscimol application affected behavioral responses and reaction times to
182 visual stimuli in a lateralized manner, suggesting that mice had adopted a strategy which relied only on
183 the presence or absence of the ipsilateral stimulus (**Extended Data Fig. 11e**, 2-way ANOVA on stimulus
184 and condition, psychometric interaction effect $p < 0.01$, reaction time condition effect $p < 0.01$). Fitting
185 kernels to predict neural activity from task events revealed that striatal visual responses were selectively
186 eliminated, sparing activity related to movement and reward licking (**Extended Data Fig. 11f**, 2-way
187 ANOVA of summed kernels on regressor and condition, stimulus kernels before muscimol > after
188 muscimol, DMS, DCS, DLS $p < 0.01$, other kernels DMS, DCS, DLS $p > 0.05$). These results indicate that, at
189 least for visual responses, striatal firing requires propagation of cortical activity rather than being
190 inherited in a cortex-independent manner from the thalamus or other regions.

191 **Striatal cell type activity**

192 The match between striatal activity and topographically aligned cortex held for medium spiny neurons
193 (MSNs) and putative parvalbumin-positive[48] fast-spiking interneurons (FSIs), but not for putative
194 cholinergic[49] tonically active neurons (TANs), which had strikingly unique and stereotyped activity (**Fig.**
195 **4**). While 95% of striatal neurons are projection medium spiny neurons (MSNs), the rest are
196 interneurons and have been proposed to have unique responses[13,21,50]. The large number of neurons
197 that we recorded combined with our ability to functionally group them by domain allowed us to test this
198 possibility rigorously. To examine task-related activity across these striatal cell types, we identified high-
199 quality single units (sorted with Kilosort, 38 ± 8% mean ± s.t.d. of clusters included, 8303/21047 units
200 total, **Extended Data Fig. 12a**) and grouped them into MSNs, FSIs, and TANs according to established
201 electrophysiological properties[51,52] (**Fig. 4a, Extended Data Fig. 12b-d**). We could also separate an
202 additional class of unidentified interneurons (UINs) previously reported[51] (**Extended Data Fig. 13**). MSNs
203 exhibited stimulus, movement and reward licking activity, firing at a range of different times during the
204 trial (**Fig. 4b, left**)**.** The proportion of cells responding to each event type differed between striatal
205 domains: nearly all stimulus-responsive cells were in DMS, most movement-onset responsive cells were
206 in DCS, and most licking-responsive cells were in DLS. Averaging the activity of MSNs in each striatal
207 domain yielded a multiunit signal that closely mimicked activity in the topographically associated regions
208 of cortex (**Figure 4c, left**). Surprisingly, given previous reports of differences[13,22,53–55], FSIs exhibited
209 similar activity to MSNs, following similar preferred events and ranges of activity patterns in each striatal
210 domain although with higher firing rates (**Fig. 4b and c, center**). In contrast, TANs had different activity:
211 they responded synchronously with a burst followed by a pause to the stimulus (in DMS and DCS) or the
212 reward (in DCS and DLS), consistent with previously observed responses but following an unexpectedly
213 strict segregation by response type and striatal location[56–59] (**Fig. 4b and c, right**). To quantify these
214 observations, we correlated the activity of individual striatal neurons with the summed activity of each
215 cell type in their domain, and with cortical widefield in the associated region. MSNs and FSIs showed
216 similar correlation with the summed activity of either class and with cortical activity in the
217 topographically aligned location, but low correlation with summed TAN activity (**Fig. 4d**, MSN, FSI, and
218 cortex similarly correlated, shuffle test for cell type and 2-way ANOVA for cortex $p > 0.05$). In contrast,
219 TANs were strongly correlated with other TANs, but weakly correlated with other cell types or with
220 cortex (**Fig. 4d**, TANs were equally less correlated to MSNs, FSIs, and cortex as themselves, 2-way
221 ANOVA $p < 0.01$). These results suggest that while MSNs and FSIs are similarly driven by cortical activity,
222 TANs are more independent, consistent with their weaker cortical input [27].

Training striatal sensory responses

Training in the task increased sensory responses in MSNs and TANs, but not in FSIs. We compared responses to visual stimuli in 5 naïve mice (n = 23 sessions) and in 11 of the trained mice in a passive context (n = 48 sessions; trials with wheel movements were excluded). Cortical responses in VISam were similar in untrained and trained mice (**Fig. 5a,c**, rank-sum test $p > 0.05$). By contrast, visual responses in the associated dorsomedial striatum were substantially larger in the trained mice (**Fig. 5b,c**, stimulus activity trained > untrained, rank-sum test $p < 0.01$). This increase affected MSNs and TANs but not FSIs, suggesting a differential effect of training across cell types (**Fig. 5c** rank-sum test, MSN and TAN $p < 0.05$, FSI > 0.05). Training also gave rise to stimulus responses in dorsocentral striatum (**Fig. 5b-d**, rank-sum test $p < 0.01$), which was likely explained by increased responses in the associated frontomedial cortex[60] (**Fig. 5a,**middle).

Discussion

By recording simultaneously across widespread areas of the cortex and along the width of the dorsal striatum, we established that activity in topographically matched regions of these two structures is remarkably similar. Furthermore, we established that the activity of most striatal neurons reflects a causal and precise influence of cortex, which is described by spatiotemporal filtering of cortical activity, is independent of task, and can be modulated but not otherwise altered by learning. The only exception to this rule of cortex over striatum was seen in the TANs (putative cholinergic interneurons[49]), which indeed receive less cortical input[27]. TAN activity may instead reflect thalamic input and dopaminergic signaling[61], consistent with recent findings that dopaminergic input to the DMS is related to contralateral stimuli and actions[62] which likely originates from the SNc.

These results indicate a dominant role for corticostriatal inputs in determining striatal responses, and raise the question of what role might be served by the remaining inputs to striatum. There are multiple input pathways to the striatum, which may shape striatal activity in unique ways. For example, specific corticostriatal projections have different arborization patterns[63], functional relevance[64], and transmitters[65]. The striatum also receives major input from the thalamus[8], which forms the dominant input onto TANs[27], can carry different stimulus information compared to cortical input[25], and can regulate behavior[24,66]. Local striatal circuitry can also pattern activity and behavior[67–69]. This complex circuitry may shape the responses of individual striatal neurons but possibly to a much lesser degree than cortical input.

Another question for further research concerns the effect of learning on striatal representations. Corticostriatal synapses are plastic, and change during learning[16,29,30]. We observed that learning substantially and specifically increased visual responses in MSNs and TANs of the dorsomedial striatum, while having little effect on FSIs. This suggests that corticostriatal synapses may gate the propagation of activity from the cortex to striatum, only strengthening to permit similar responses in the cortex and striatum when particular cortical activity becomes relevant to behavior. As striatal visual responses were not related to the upcoming choice of movement, and also occurred strongly during passive stimulus presentation in trained mice, this increased activity appears to reflect increased transmission of sensory activity, rather than a movement command evoked by the stimulus.

An important step in future research will be to understand how the cortical signals are modified from the striatum to downstream basal ganglia targets. For example, while activity in the striatal direct and indirect pathways are correlated[70], they have different functions[71–74] and plasticity[30] and likely shape downstream targets in complementary ways. The loop architecture between the cortex, basal ganglia, thalamus and back to cortex also implies that striatal activity can in turn shape cortical activity, possibly reflecting the functional importance of shared responses[33,75]. We have here introduced new

experimental and computational approaches to demonstrate how activity of specific striatal cell types and domains precisely reflects causal and topographic cortical activity. We hope that these approaches will help shed light on the broader question of signal propagation across the multiple pathways through the basal ganglia.

References

1. Kim, H. F. & Hikosaka, O. Distinct Basal Ganglia Circuits Controlling Behaviors Guided by Flexible and Stable Values. *Neuron* **79,** 1001–1010 (2013).

2. Wang, L., Rangarajan, K. V., Gerfen, C. R. & Krauzlis, R. J. Activation of Striatal Neurons Causes a Perceptual Decision Bias during Visual Change Detection in Mice. *Neuron* **97,** 1369-1381.e5 (2018).

3. Guo, L., Walker, W. I., Ponvert, N. D., Penix, P. L. & Jaramillo, S. Stable representation of sounds in the posterior striatum during flexible auditory decisions. *Nat. Commun.* **9,** 1534 (2018).

4. Rueda-Orozco, P. E. & Robbe, D. The striatum multiplexes contextual and kinematic information to constrain motor habits execution. *Nat. Neurosci.* **18,** 453–460 (2015).

5. Yartsev, M. M., Hanks, T. D., Yoon, A. M. & Brody, C. D. Causal contribution and dynamical encoding in the striatum during evidence accumulation. *Elife* **7,** 245316 (2018).

6. Tai, L.-H., Lee, a M., Benavidez, N., Bonci, A. & Wilbrecht, L. Transient stimulation of distinct subpopulations of striatal neurons mimics changes in action value. *Nat. Neurosci.* **15,** 1281–9 (2012).

7. Hintiryan, H., Foster, N. N., Bowman, I., Bay, M., Song, M. Y., Gou, L., Yamashita, S., Bienkowski, M. S., Zingg, B., Zhu, M., Yang, X. W., Shih, J. C., Toga, A. W. & Dong, H.-W. The mouse cortico-striatal projectome. *Nat. Neurosci.* **19,** 1100–1114 (2016).

8. Hunnicutt, B. J., Jongbloets, B. C., Birdsong, W. T., Gertz, K. J., Zhong, H. & Mao, T. A comprehensive excitatory input map of the striatum reveals novel functional organization. *Elife* **5,** 1–32 (2016).

9. Friedman, A., Homma, D., Gibb, L. G. G., Amemori, K., Rubin, S. J. J., Hood, A. S. S., Riad, M. H. H. & Graybiel, A. M. M. A Corticostriatal Path Targeting Striosomes Controls Decision-Making under Conflict. *Cell* **161,** 1320–1333 (2015).

10. Gremel, C. M., Chancey, J. H., Atwood, B. K., Luo, G., Neve, R., Ramakrishnan, C., Deisseroth, K., Lovinger, D. M. & Costa, R. M. Endocannabinoid Modulation of Orbitostriatal Circuits Gates Habit Formation. *Neuron* **90,** 1312–1324 (2016).

11. Znamenskiy, P. & Zador, A. M. Corticostriatal neurons in auditory cortex drive decisions during auditory discrimination. *Nature* **497,** 482–5 (2013).

12. Fujii, N. & Graybiel, A. M. Time-varying covariance of neural activities recorded in striatum and frontal cortex as monkeys perform sequential-saccade tasks. *Proc. Natl. Acad. Sci.* **102,** 9032–9037 (2005).

13. Martiros, N., Burgess, A. A. & Graybiel, A. M. Inversely Active Striatal Projection Neurons and Interneurons Selectively Delimit Useful Behavioral Sequences. *Curr. Biol.* **0,** 1–14 (2018).

14. Buch, E. R., Brasted, P. J. & Wise, S. P. Comparison of population activity in the dorsal premotor cortex and putamen during the learning of arbitrary visuomotor mappings. *Exp. brain Res.* **169,** 69–84 (2006).

15. Pidoux, M., Mahon, S., Deniau, J. M. & Charpier, S. Integration and propagation of somatosensory responses in the corticostriatal pathway: An intracellular study in vivo. *J. Physiol.* **589,** 263–281 (2011).

16. Xiong, Q., Znamenskiy, P. & Zador, A. M. Selective corticostriatal plasticity during acquisition of an auditory discrimination task. *Nature* **521,** 348–351 (2015).

17. Kincaid, A. E., Zheng, T. & Wilson, C. J. Connectivity and convergence of single corticostriatal axons. *J. Neurosci.* **18,** 4722–4731 (1998).

18. Huerta-Ocampo, I., Mena-Segovia, J. & Bolam, J. P. Convergence of cortical and thalamic input to direct and indirect pathway medium spiny neurons in the striatum. *Brain Struct. Funct.* **219,** 1787–1800 (2014).

19. Emmons, E. B., De Corte, B. J., Kim, Y., Parker, K. L., Matell, M. S. & Narayanan, N. S. Rodent medial frontal control of temporal processing in the dorsomedial striatum. *J. Neurosci.* **37,** 1376–17 (2017).

20. Lemke, S. M., Ramanathan, D. S., Guo, L., Won, S. J. & Ganguly, K. Emergent modular neural control drives coordinated motor actions. *Nat. Neurosci.* **22,** 1122–1131 (2019).

21. Apicella, P. Tonically active neurons in the primate striatum and their role in the processing of information about motivationally relevant events. *Eur. J. Neurosci.* **16,** 2017–2026 (2002).

22. Gage, G. J., Stoetzner, C. R., Wiltschko, A. B. & Berke, J. D. Selective Activation of Striatal Fast-Spiking Interneurons during Choice Execution. *Neuron* **67,** 466–479 (2010).

23. Stalnaker, T. A., Berg, B., Aujla, N. & Schoenbaum, G. Cholinergic Interneurons Use Orbitofrontal Input to Track Beliefs about Current State. *J. Neurosci.* **36,** 6242–57 (2016).

24. Kato, S., Kuramochi, M., Kobayashi, K., Fukabori, R., Okada, K., Uchigashima, M., Watanabe, M., Tsutsui, Y. & Kobayashi, K. Selective Neural Pathway Targeting Reveals Key Roles of Thalamostriatal Projection in the Control of Visual Discrimination. *J. Neurosci.* **31,** 17169–17179 (2011).

25. Ponvert, N. D. & Jaramillo, S. Auditory Thalamostriatal and Corticostriatal Pathways Convey Complementary Information about Sound Features. *J. Neurosci.* **39,** 271–280 (2019).

26. Bolam, J. P., Hanley, J. J., Booth, P. A. C. & Bevan, M. D. Synaptic organisation of the basal ganglia. *J. Anat.* **196,** 527–542 (2000).

27. Johansson, Y. & Silberberg, G. The Functional Organization of Cortical and Thalamic Inputs onto Five Types of Striatal Neurons Is Determined by Source and Target Cell Identities. *Cell Rep.* **30,** 1178-1194.e3 (2020).

28. Burke, D. A., Rotstein, H. G. & Alvarez, V. A. Striatal Local Circuitry: A New Framework for Lateral Inhibition. *Neuron* **96,** 267–284 (2017).

29. O'Hare, J. K., Ade, K. K., Sukharnikova, T., Van Hooser, S. D., Palmeri, M. L., Yin, H. H. & Calakos, N. Pathway-Specific Striatal Substrates for Habitual Behavior. *Neuron* **89,** 472–479 (2016).

30. Rothwell, P. E., Hayton, S. J., Sun, G. L., Fuccillo, M. V., Lim, B. K. & Malenka, R. C. Input- and Output-Specific Regulation of Serial Order Performance by Corticostriatal Circuits. *Neuron* **88,** 345–356 (2015).

31. Costa, R., Cohen, D. & Nicolelis, M. Differential corticostriatal plasticity during fast and slow motor skill learning in mice. *Curr. Biol. CB* **14,** 1124–1134 (2004).

32. Pasupathy, A. & Miller, E. K. Different time courses of learning-related activity in the prefrontal cortex and striatum. *Nature* **433,** 873–6 (2005).

33. Koralek, A. C., Jin, X., Long II, J. D., Costa, R. M. & Carmena, J. M. Corticostriatal plasticity is necessary for learning intentional neuroprosthetic skills. *Nature* **483,** 331–335 (2012).

34. Koralek, A. C., Costa, R. M. & Carmena, J. M. Temporally precise cell-specific coherence develops in corticostriatal networks during learning. *Neuron* **79,** 865–72 (2013).

35. Barnes, T. D., Kubota, Y., Hu, D., Jin, D. Z. & Graybiel, A. M. Activity of striatal neurons reflects dynamic encoding and recoding of procedural memories. *Nature* **437,** 1158–61 (2005).

36. Jin, X. & Costa, R. M. Start/stop signals emerge in nigrostriatal circuits during sequence learning. *Nature* **466,** 457–62 (2010).

37. Oh, S. W., Harris, J. a, Ng, L., Winslow, B., Cain, N., Mihalas, S., Wang, Q., Lau, C., Kuan, L., Henry, A. M., Mortrud, M. T., Ouellette, B., Nguyen, T. N., Sorensen, S. a, Slaughterbeck, C. R., Wakeman, W., Li, Y., Feng, D., Ho, A., *et al.* A mesoscale connectome of the mouse brain. *Nature* **508,** 207–14 (2014).

38. Choi, E. Y., Yeo, B. T. T. & Buckner, R. L. The organization of the human striatum estimated by intrinsic functional connectivity. *J. Neurophysiol.* **108,** 2242–2263 (2012).

39. Burgess, C. P., Lak, A., Steinmetz, N. A., Zatka-Haas, P., Bai Reddy, C., Jacobs, E. A. K., Linden, J. F., Paton, J. J., Ranson, A., Schröder, S., Soares, S., Wells, M. J., Wool, L. E., Harris, K. D. & Carandini, M. High-Yield Methods for Accurate Two-Alternative Visual Psychophysics in Head-Fixed Mice. *Cell Rep.* **20,** 2513–2524 (2017).

40. Wekselblatt, J. B., Flister, E. D., Piscopo, D. M. & Niell, C. M. Large-scale imaging of cortical dynamics during sensory perception and behavior. *J. Neurophysiol.* **115,** 2852–2866 (2016).

41. Jun, J. J., Steinmetz, N. A., Siegle, J. H., Denman, D. J., Bauza, M., Barbarits, B., Lee, A. K., Anastassiou, C. A., Andrei, A.,

Aydın, Ç., Barbic, M., Blanche, T. J., Bonin, V., Couto, J. J., Dutta, B., Gratiy, S. L., Gutnisky, D. A., Häusser, M., Karsh, B., *et al.* Fully integrated silicon probes for high-density recording of neural activity. *Nature* **in press,** 232–236 (2017).

42. Sakata, S. & Harris, K. D. Laminar Structure of Spontaneous and Sensory-Evoked Population Activity in Auditory Cortex. *Neuron* **64,** 404–418 (2009).

43. Beaulieu-Laroche, L., Toloza, E. H. S., Brown, N. J. & Harnett, M. T. Widespread and Highly Correlated Somato-dendritic Activity in Cortical Layer 5 Neurons. *Neuron* **103,** 235-241.e4 (2019).

44. Allen, W. E., Kauvar, I. V., Chen, M. Z., Richman, E. B., Yang, S. J., Chan, K., Gradinaru, V., Deverman, B. E., Luo, L. & Deisseroth, K. Global Representations of Goal-Directed Behavior in Distinct Cell Types of Mouse Neocortex. *Neuron* **94,** 891-907.e6 (2017).

45. Shepherd, G. M. G. Corticostriatal connectivity and its role in disease. *Nat. Rev. Neurosci.* **14,** 278–291 (2013).

46. Einstein, M. C., Polack, P.-O., Tran, D. T. & Golshani, P. Visually Evoked 3–5 Hz Membrane Potential Oscillations Reduce the Responsiveness of Visual Cortex Neurons in Awake Behaving Mice. *J. Neurosci.* **37,** 5084–5098 (2017).

47. Jacobs, E. A. K., Steinmetz, N. A., Carandini, M., Harris, K. D. & Uk, K. Cortical state fluctuations during sensory decision making. *bioRxiv* 1–22 (2017). doi:10.1101/348193

48. Mallet, N., Le Moine, C., Charpier, S. & Gonon, F. Feedforward inhibition of projection neurons by fast-spiking GABA interneurons in the rat striatum in vivo. *J. Neurosci.* **25,** 3857–3869 (2005).

49. Inokawa, H., Yamada, H., Matsumoto, N., Muranishi, M. & Kimura, M. Juxtacellular labeling of tonically active neurons and phasically active neurons in the rat striatum. *Neuroscience* **168,** 395–404 (2010).

50. Berke, J. D. Functional properties of striatal fast-spiking interneurons. *Front. Syst. Neurosci.* **5,** 1–7 (2011).

51. Yamin, H. G., Stern, E. A. & Cohen, D. Parallel processing of environmental recognition and locomotion in the mouse striatum. *J. Neurosci.* **33,** 473–84 (2013).

52. Schmitzer-Torbert, N. C. & Redish, A. D. Task-dependent encoding of space and events by striatal neurons is dependent on neural subtype. *Neuroscience* **153,** 349–360 (2008).

53. Berke, J. D. Uncoordinated firing rate changes of striatal fast-spiking interneurons during behavioral task performance. *J. Neurosci.* **28,** 10075–10080 (2008).

54. Kim, N., Li, H. E., Hughes, R. N., Watson, G. D. R., Gallegos, D., West, A. E., Kim, I. H. & Yin, H. H. A striatal interneuron circuit for continuous target pursuit. *Nat. Commun.* **10,** 2715 (2019).

55. Yamada, H., Inokawa, H., Hori, Y., Pan, X., Matsuzaki, R., Nakamura, K., Samejima, K., Shidara, M., Kimura, M., Sakagami, M. & Minamimoto, T. Characteristics of fast-spiking neurons in the striatum of behaving monkeys. *Neurosci. Res.* **105,** 2–18 (2016).

56. Aosaki, T., Tsubokawa, H., Ishida, a, Watanabe, K., Graybiel, a M. & Kimura, M. Responses of tonically active neurons in the primate's striatum undergo systematic changes during behavioral sensorimotor conditioning. *J. Neurosci.* **14,** 3969–3984 (1994).

57. Benhamou, L., Kehat, O. & Cohen, D. Firing pattern characteristics of tonically active neurons in rat striatum: context dependent or species divergent? *J. Neurosci.* **34,** 2299–304 (2014).

58. Apicella, P. The role of the intrinsic cholinergic system of the striatum: What have we learned from TAN recordings in behaving animals ? *Neuroscience* **360,** 81–94 (2017).

59. Marche, K., Martel, A.-C. & Apicella, P. Differences between Dorsal and Ventral Striatum in the Sensitivity of Tonically Active Neurons to Rewarding Events. *Front. Syst. Neurosci.* **11,** 1–12 (2017).

60. Orsolic, I., Rio, M., Mrsic-Flogel, T. D. & Znamenskiy, P. Mesoscale cortical dynamics reflect the interaction of sensory evidence and temporal expectation during perceptual decision-making. *bioRxiv* 552026 (2019). doi:10.1101/552026

61. Threlfell, S., Lalic, T., Platt, N. J., Jennings, K. A., Deisseroth, K. & Cragg, S. J. Striatal dopamine release is triggered by synchronized activity in cholinergic interneurons. *Neuron* **75,** 58–64 (2012).

62. Moss, M., Zatka-Haas, P., Harris, K., Carandini, M. & Lak, A. Dopamine axons to dorsal striatum encode contralateral stimuli and actions. 1–12 (2020). doi:10.1101/2020.07.16.207316

63. Hooks, B. M., Papale, A. E., Paletzki, R. F., Feroze, M. W., Eastwood, B. S., Couey, J. J., Winnubst, J., Chandrashekar, J. &

Gerfen, C. R. Topographic precision in sensory and motor corticostriatal projections varies across cell type and cortical area. *Nat. Commun.* **9,** 3549 (2018).

64. Reig, R. & Silberberg, G. Distinct Corticostriatal and Intracortical Pathways Mediate Bilateral Sensory Responses in the Striatum. *Cereb. Cortex* 1–11 (2016). doi:10.1093/cercor/bhw268

65. Rock, C., Zurita, H., Wilson, C. & Apicella, A. J. An inhibitory corticostriatal pathway. *Elife* **5,** 1–17 (2016).

66. Kato, S., Fukabori, R., Nishizawa, K., Okada, K., Yoshioka, N., Sugawara, M., Maejima, Y., Shimomura, K., Okamoto, M., Eifuku, S. & Kobayashi, K. Action Selection and Flexible Switching Controlled by the Intralaminar Thalamic Neurons. *Cell Rep.* **22,** 2370–2382 (2018).

67. Holly, E. N., Davatolhagh, M. F., Choi, K., Alabi, O. O., Vargas Cifuentes, L. & Fuccillo, M. V. Striatal Low-Threshold Spiking Interneurons Regulate Goal-Directed Learning. *Neuron* **103,** 92-101.e6 (2019).

68. Lee, K., Holley, S. M., Shobe, J. L., Chong, N. C., Cepeda, C., Levine, M. S. & Masmanidis, S. C. Parvalbumin Interneurons Modulate Striatal Output and Enhance Performance during Associative Learning. *Neuron* **93,** 1451-1463.e4 (2017).

69. Gritton, H. J., Howe, W. M., Romano, M. F., DiFeliceantonio, A. G., Kramer, M. A., Saligrama, V., Bucklin, M. E., Zemel, D. & Han, X. Unique contributions of parvalbumin and cholinergic interneurons in organizing striatal networks during movement. *Nat. Neurosci.* **22,** (2019).

70. Markowitz, J. E., Gillis, W. F., Beron, C. C., Linderman, S. W., Sabatini, B. L. & Datta Correspondence, S. R. The Striatum Organizes 3D Behavior via Moment-to- Moment Action Selection Normal syllable sequence Lesion Syllable A. *Cell* **174,** 1–15 (2018).

71. Tecuapetla, F., Jin, X., Lima, S. Q. & Costa, R. M. Complementary Contributions of Striatal Projection Pathways to Action Initiation and Execution. *Cell* **166,** 703–715 (2016).

72. Geddes, C. E., Li, H. & Jin, X. Optogenetic Editing Reveals the Hierarchical Organization of Learned Action Sequences. *Cell* **174,** 32-43.e15 (2018).

73. Kravitz, A. V, Freeze, B. S., Parker, P. R. L., Kay, K., Thwin, M. T., Deisseroth, K. & Kreitzer, A. C. Regulation of parkinsonian motor behaviours by optogenetic control of basal ganglia circuitry. *Nature* **466,** 622–6 (2010).

74. Yttri, E. A. & Dudman, J. T. Opponent and bidirectional control of movement velocity in the basal ganglia. *Nature* 1–16 (2016). doi:10.1038/nature17639

75. Neely, R. M., Koralek, A. C., Athalye, V. R., Costa, R. M. & Carmena, J. M. Volitional Modulation of Primary Visual Cortex Activity Requires the Basal Ganglia. *Neuron* **97,** 1356-1368.e4 (2018).

Acknowledgements

We thank C. Reddy, M. Wells, L. Funnell, and H. Forrest for mouse husbandry and training, R. Raghupathy for histology, D. Cohen for helpful discussions, and the NVIDIA Corporation for donation of a Titan X GPU. This work was supported by a Newton International Fellowship, EMBO Fellowship (ALTF 1428-2015), and a Human Frontier Science Program Fellowship (LT226/2016-L) to A.J.P, a Wellcome Trust PhD Studentship to JMJF, a Human Frontier Science Program Fellowship (LT001071/2015-L) and Marie Skłodowska-Curie fellowship of the E.U. Horizon 2020 (656528) to N.A.S., Wellcome Trust grants 205093, 204915 to K.DH. and M.C, ERC grant 694401 to K.D.H, M.C. holds the GlaxoSmithKline / Fight for Sight Chair in Visual Neuroscience.

Author Contributions

AJP, KDH, and MC conceived and designed the study. AJP collected and analyzed data, JMJF analyzed cell types and single-unit data, NAS developed widefield imaging and Neuropixels setups. AJP, KDH, and MC wrote the manuscript with input from JMJF and NAS.

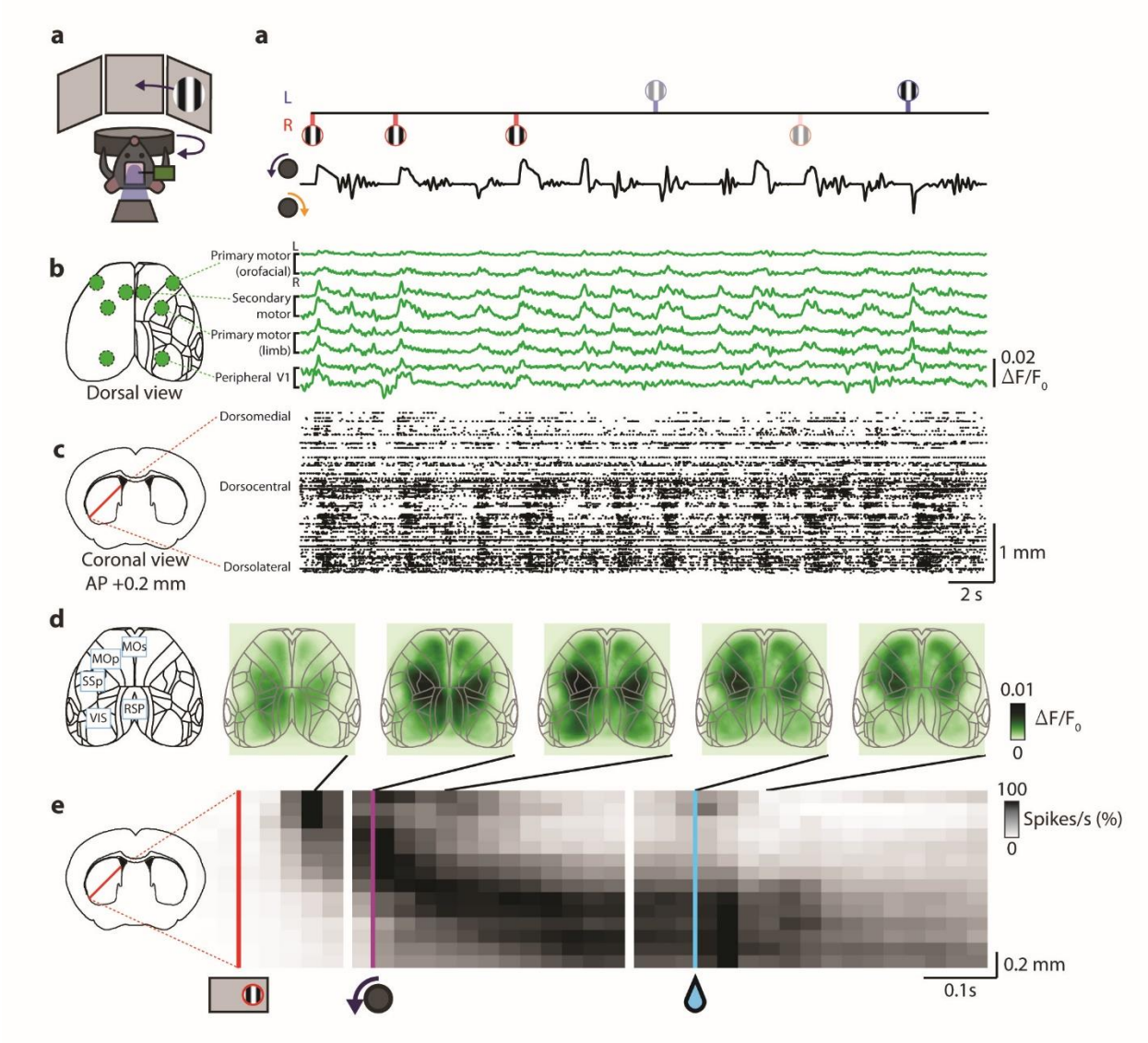

Figure 1 | Cortex and striatum show spatial gradients of sensorimotor activity during visually guided behavior. **a,** Left, task setup; right, time trace illustrating task events from an example session. Gratings either side of the top line indicate stimulus onset times, located above or below the time axis according to their position, and shaded according to their contrast. Bottom trace indicates wheel velocity. **b,** Cortical activity measured by widefield calcium imaging during the same time period as in (b). Deconvolved fluorescence traces are shown for four regions of interest on both sides: secondary motor cortex (MOs), primary motor cortex (MOp, orofacial and limb) and primary visual cortex (VISp). **c,** Spikes measured simultaneously across dorsal striatum during the same time period. **d**, Deconvolved cortical fluorescence maps, averaged at four timepoints over all trials of all recordings with right-hand stimuli, correct counterclockwise wheel turns, and < 500 ms reaction times. MOs: secondary motor cortex; MOp: primary motor cortex; SSp: Primary somatosensory cortex; VIS: visual cortex; RSP: retrosplenial cortex. **e,** Mean multiunit firing rate in striatum as a function of depth and time, averaged over the same events as in (d). The three grayscale panels (separated by white vertical lines) represent activity temporally aligned to visual stimulus onset (red line); contralaterally-orienting movements (purple line), and rewards (blue line). Firing rates are arranged by depth from the lateral striatal border, averaged across sessions, and max-normalized.

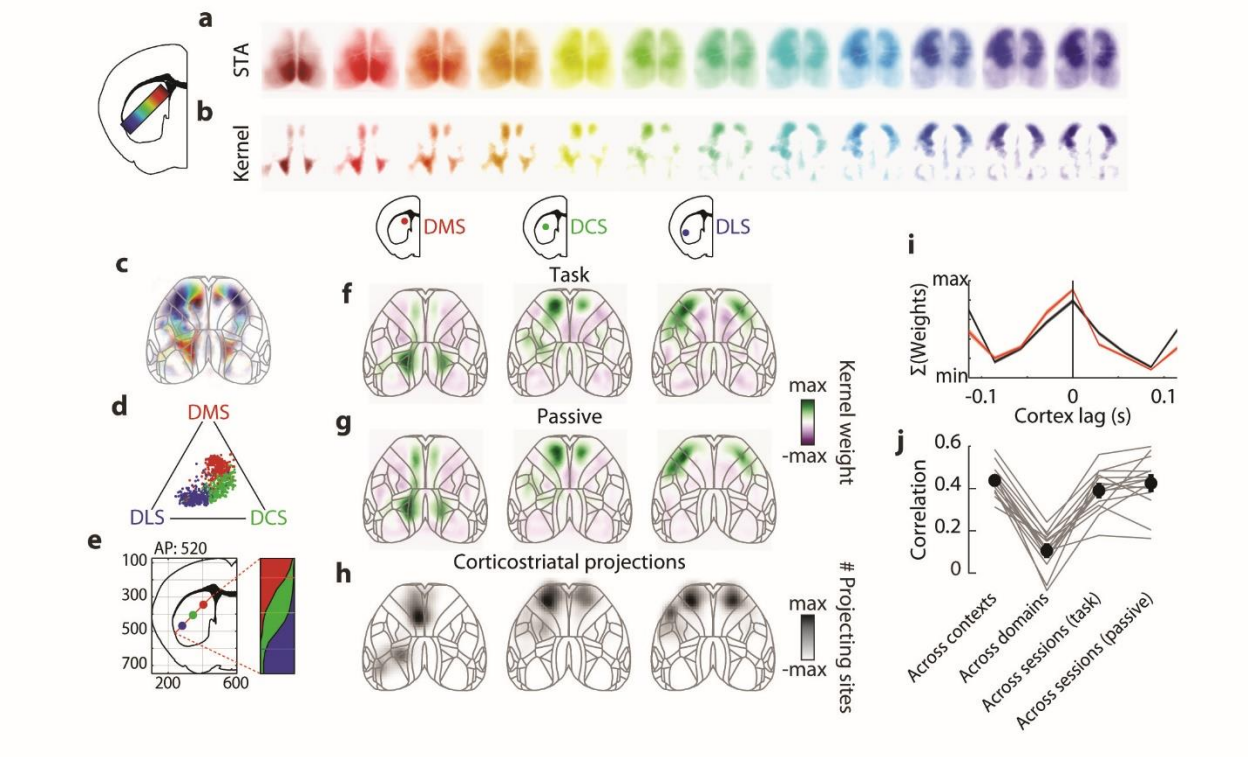

Figure 2 | Striatal domains are topographically correlated with connected cortical regions. a, Spike-triggered average of cortical fluorescence measured for multiunit activity at each striatal location (colors), averaged across sessions from all mice. **b**, Corresponding spatial kernels, which best predict striatal multiunit activity from cortical fluorescence. **c,** Superimposition the kernel weights in (b) colored by striatal location. **d,** Ternary plot showing correlations of the cortical kernel associated with each 200 µm segment of striatum, with the three template kernels used to assign each segment to a striatal domain. Vertices represent maximum correlation with one template and minimum correlation with the other two. The progression of templates across striatal depth is continuous, but divided into three domains for further analysis. **e,** Left, CCF coordinates for each striatal domain (mean across recorded locations); right, probability of domain categorization as a function of striatal location. The y-axis represents depth along the striatal electrode; the three colors at each depth represent the fraction of segments from that depth that were assigned to each of the three striatal domains, across all recording sessions. **f**, Mean cortical spatial kernels for each striatal domain (lag = 0 s) during the task, averaged across sessions. **g**, Cortical spatial kernels as in (f) but computed while mice passively viewed random dot stimuli. **h,** Density of cortical locations projecting to each striatal domain, data from the Allen connectivity database[37]. **i,** Time course of weights predicting striatal from cortical activity, summed across pixels after computing spatiotemporal kernels. Black: kernels in task performance; red: passive visual random dot stimuli (mean across domains and sessions ± s.e.m across sessions). The sum of weights for cortex leading striatum is greater than the cortex lagging striatum (signed-rank test, $p = 2.5*10^{-6}$ across 77 sessions), consistent with propagation of activity from cortex to striatum. **j,** Correlation of spatiotemporal cortical kernels across contexts (task or passive, in the same striatal domain and recording session), across striatal domains (in the same task and session), and across sessions during the task and in the passive condition (in the same striatal domain) (mean ± s.e.m across mice). Cortical kernels fit from different behavioral contexts or recording sessions are highly correlated, but kernels fit from different striatal domains are significantly less correlated (signed-rank test, $p = 6.1*10^{-5}$ across 15 mice), indicating regional specificity.

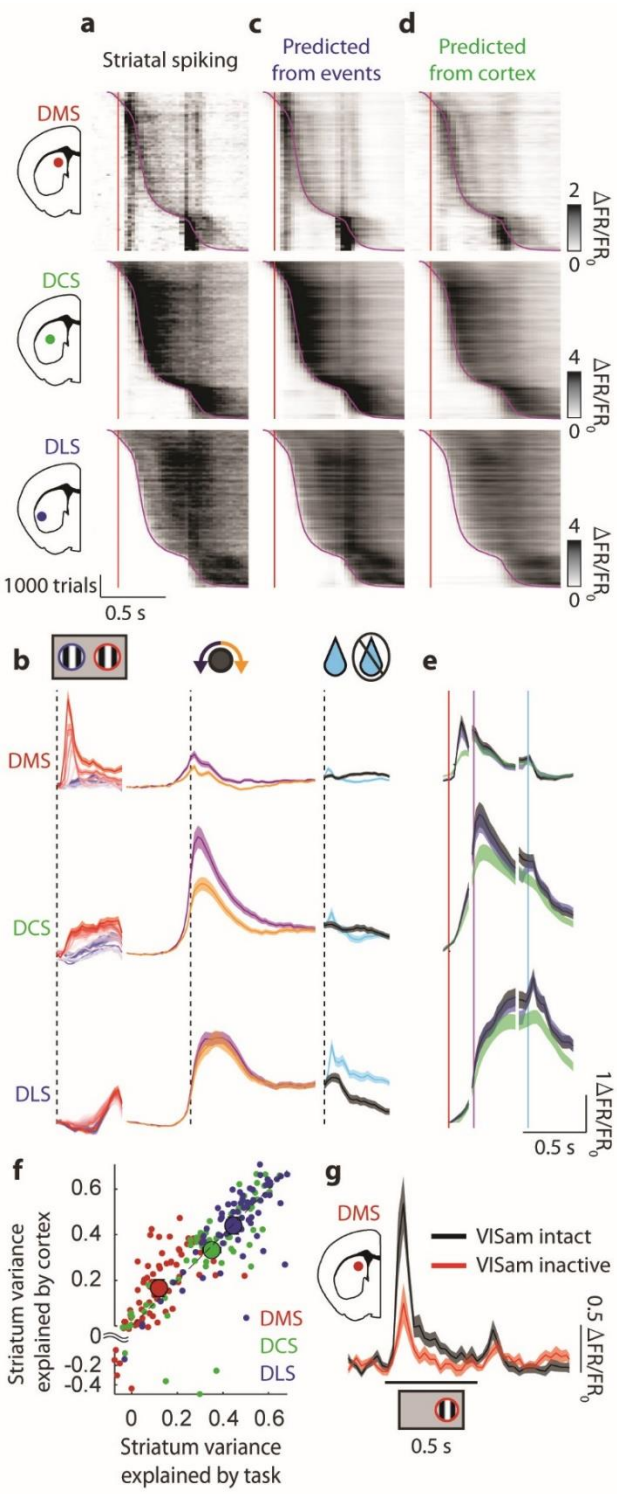

Figure 3 | Striatal sensorimotor activity reflects associated cortical activity. a, Mean population activity within each striatal domain, shown for all trials with contralateral stimuli, contralaterally-orienting movements, and rewards. Trials are combined across sessions and sorted by reaction time (time of movement onset). Red line: stimulus onset, purple curve: movement onset. For graphical purposes, activity at each time is smoothed with a running average of 100 trials to highlight features that are consistent across trials. **b,** Temporal kernels predicting activity in each striatal domain from task events. Left column: blue and red curves show kernels for ipsilateral and contralateral stimuli of different contrasts, indicated by color saturation. Middle column: kernels for contralateral-orienting and ipsilateral-orienting movements (purple and orange). Right column: kernels for reward (cyan), and reward omission (black). Vertical black dotted lines indicate event onset, shading indicates mean ± s.e.m across sessions. **c,** Prediction of firing rate in each striatal domain obtained from task events, formatted as in (a). **d,** Prediction of striatal firing rate from cortical activity, formatted as in (a). **e,** Trial-averaged activity in each striatal domain (black), predicted from task events (blue), and predicted from cortical activity (green), aligned to stimulus (red line), movement (purple line), and reward (cyan line) (mean ± s.e.m across sessions). **f,** Cross-validated explained variance (R^2) of striatal activity predicted from the cortex and task. Small dots, sessions; large dots, mean across sessions. The cortex explains more or the same amount of striatal activity as task events, indicating that striatal activity mirrors cortical activity (signed-rank test, $p_{DMS} = 5.8*10^{-4}$, $p_{DCS} = 0.17$, $p_{DLS} = 0.48$). **g,** Passive responses to visual stimuli in the DMS before (black) and after (red) inactivation of VISam with muscimol.

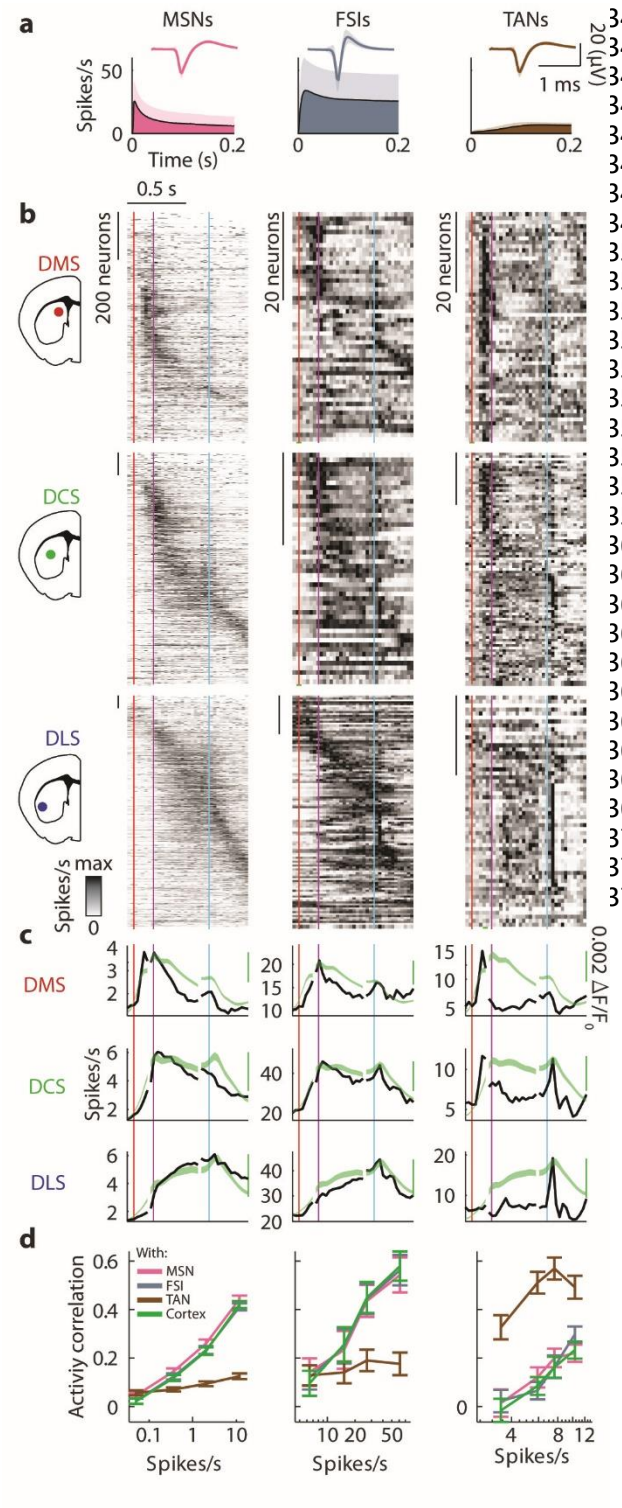

Figure 4 | Striatal mirroring of cortical activity is cell-type specific. a, Waveforms and autocorrelelograms used to define striatal cells as medium spiny neurons (MSNs), fast spiking interneurons (FSIs), and tonically active neurons (TANs) (mean ± s.t.d. across cells). **b,** Spikes of individual cells of each class aligned to contralateral stimuli (red lines), contralaterally-orienting movements (purple vertical lines), and rewards (blue vertical lines), averaged across trials with reaction times less than 500 ms, max-normalized, and sorted by time of maximum activity using half of the trials and plotting the other half of trials. Rows correspond to striatal domains, columns to cell types. **c,** Activity as in (b) averaged across neurons of each cell type and domain (black traces). For reference, each row reports the cortical activity within a region of cortex associated with each domain (green), providing a good prediction of MSN and FSN activity but not of TAN activity. **d,** Correlations of individual neurons for each domain and cell type with the average activity of each cell type in that striatal domain, or with activity of the topographically aligned cortical ROI (mean ± s.e.m. across sessions). MSNs and FSIs were equally correlated with themselves as with each other (shuffling MSN/FSI labels within sessions, MSN: $p = 0.47$, FSI: $p = 0.99$ across 77 recordings), or with cortical activity (2-way ANOVA on firing rate and type, type effect: MSN $p = 0.94$, FSI $p = 0.88$ across 77 recordings). TANS were correlated with themselves and equally uncorrelated to MSNs, FSIs, and cortical activity (2-way ANOVA on firing rate and type, TAN vs MSN $p = 7.5*10^{-48}$, TAN vs FSI $p = 2.0*10^{-6}$, TAN vs MSN, FSI, and cortex $p = 0.68$ across 77 recordings).

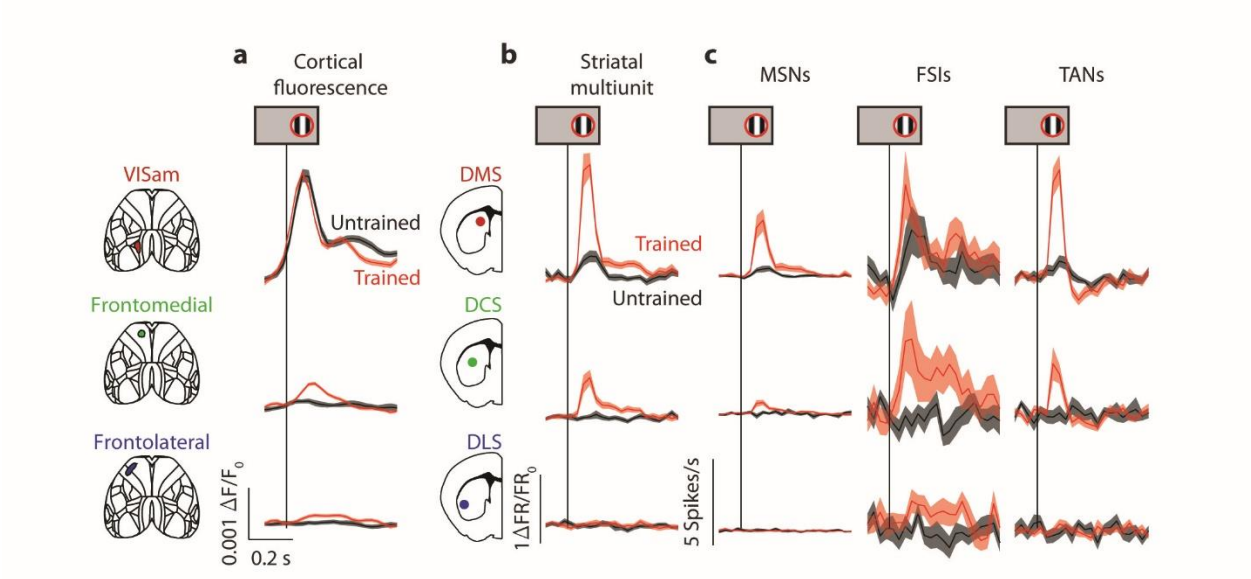

Figure 5| Striatal stimulus responses increase independently from visual cortex after training. a, Cortical activity within ROIs associated with each striatal domain in untrained (black) and trained (red) mice to 100% contrast contralateral stimuli (mean ± s.e.m across sessions). Stimulus responses within visual area VISam do not change with training but increase in the frontomedial cortex (rank-sum test, VISam: $p = 0.08$, frontomedial: $p = 6.2*10^{-3}$ across 23 untrained and 48 trained sessions). **b,** Striatal activity, plotted as in (a). Stimulus responses increases in the dorsomedial striatum and dorsocentral striatum (rank-sum test, DMS: $p = 2.1*10^{-4}$, DCS: $p = 9.7*10^{-4}$, time window 0-0.2 s). **c,** Striatal activity as in (a) within each cell type. Stimulus activity within the dorsomedial and dorsocentral striatum increases for MSNs and TANs but not for FSIs (rank-sum test, DMS: MSN $p = 2.8*10^{-3}$, FSI $p = 0.32$, TAN $p = 0.013$, time window 0-0.2 s from stimulus onset).

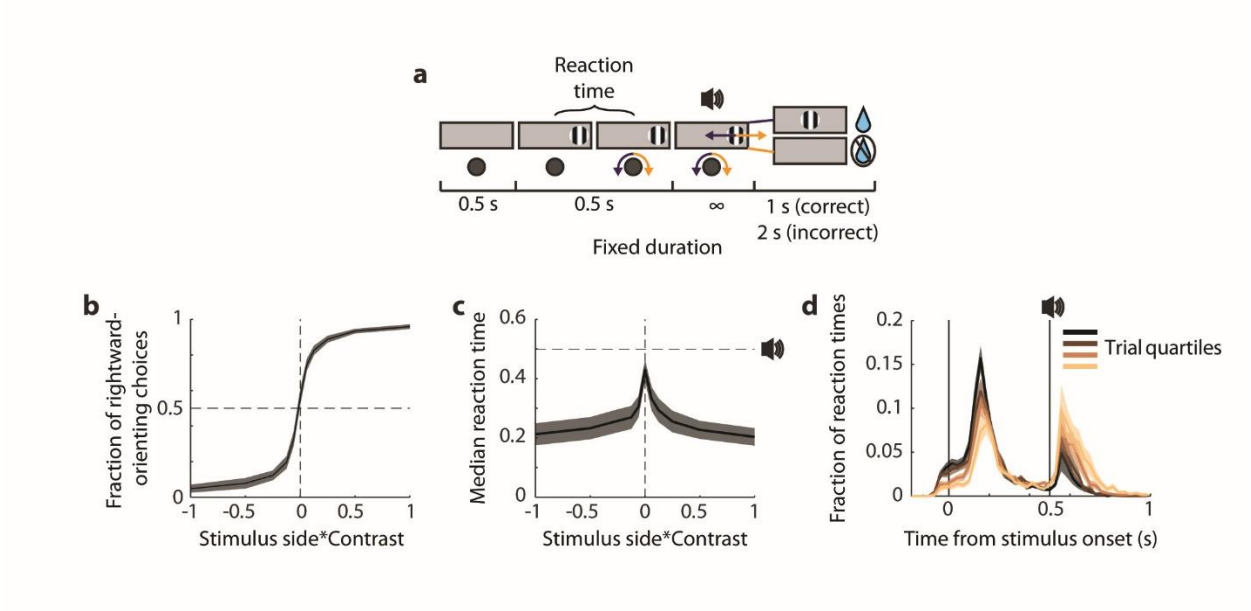

Extended Data Figure 1 |Task performance. a, Timeline of events in a trial. After 0.5 s with no wheel movement, a stimulus appears. The mouse may turn the wheel immediately, but it only becomes yoked to the stimulus after a further 0.5 s, at which time an auditory Go cue is played. If the mouse drives the stimulus into the center, a water reward is delivered and a new trial begins after 1s; if the mouse drives the stimulus off the screen away from the center, a white noise sound is played and a new trial begins after 2 s. **b,** Psychometric curve showing task performance: the fraction of choices as a function of stimulus contrast and side (left-hand stimuli are negative, right-hand stimuli are positive). Curve and shaded region show mean ± s.e.m. across sessions. **c,** Median reaction time as a function of stimulus contrast and side as in (b) (mean ± s.e.m. across each session's median). **d,** Histogram of times from stimulus to movement onset by trial quartile within sessions (first quarter of trials in the session in black, last quarter in beige; mean ± s.e.m. across mice). In early trials, mice typically begin moving the wheel before the Go cue. Later in the sessions, they often waited for the Go cue.

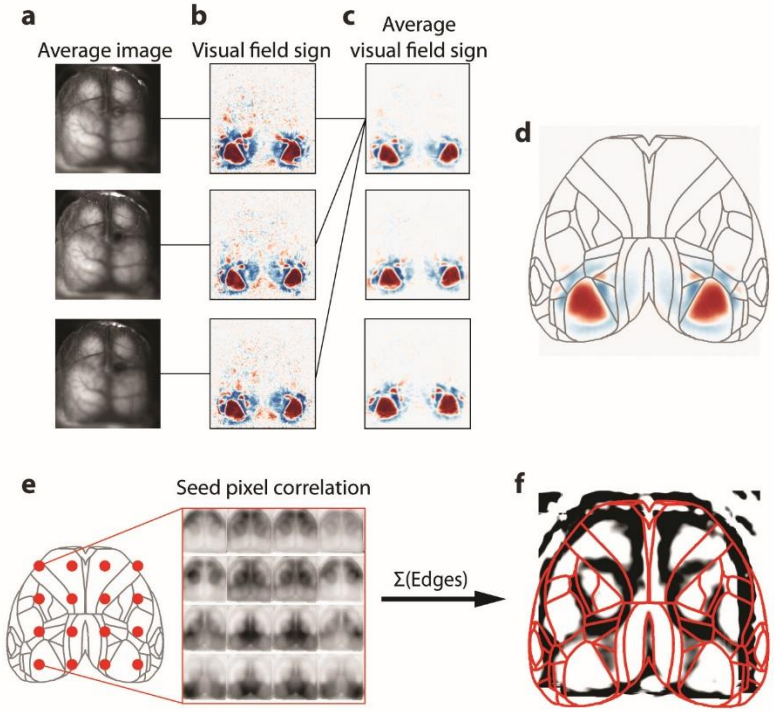

Extended Data Figure 2 | Cortical widefield alignment. a, Example widefield images from one mouse, used to align vasculature. **b,** Retinotopic visual field sign maps corresponding to the sessions in (a). **c,** Retinotopic maps averaged across all sessions for three example mice, used to align widefield images across mice. **d,** Retinotopic map averaged across mice and symmetrized, used to align to the Allen CCF atlas. **e,** Example cortical seed pixels (left) used to create pixel-pixel correlation maps (right). **f,** Pixel-pixel correlation maps as in (e) edge-filtered and summed with overlaid Allen CCF cortical regions. These correlation edges demarcate correlated regions (e.g. visual cortex posterior, motor cortex anterior) and line up with Allen CCF regions, indicating that our alignment methods based on retinotopy also successfully align anterior cortical regions.

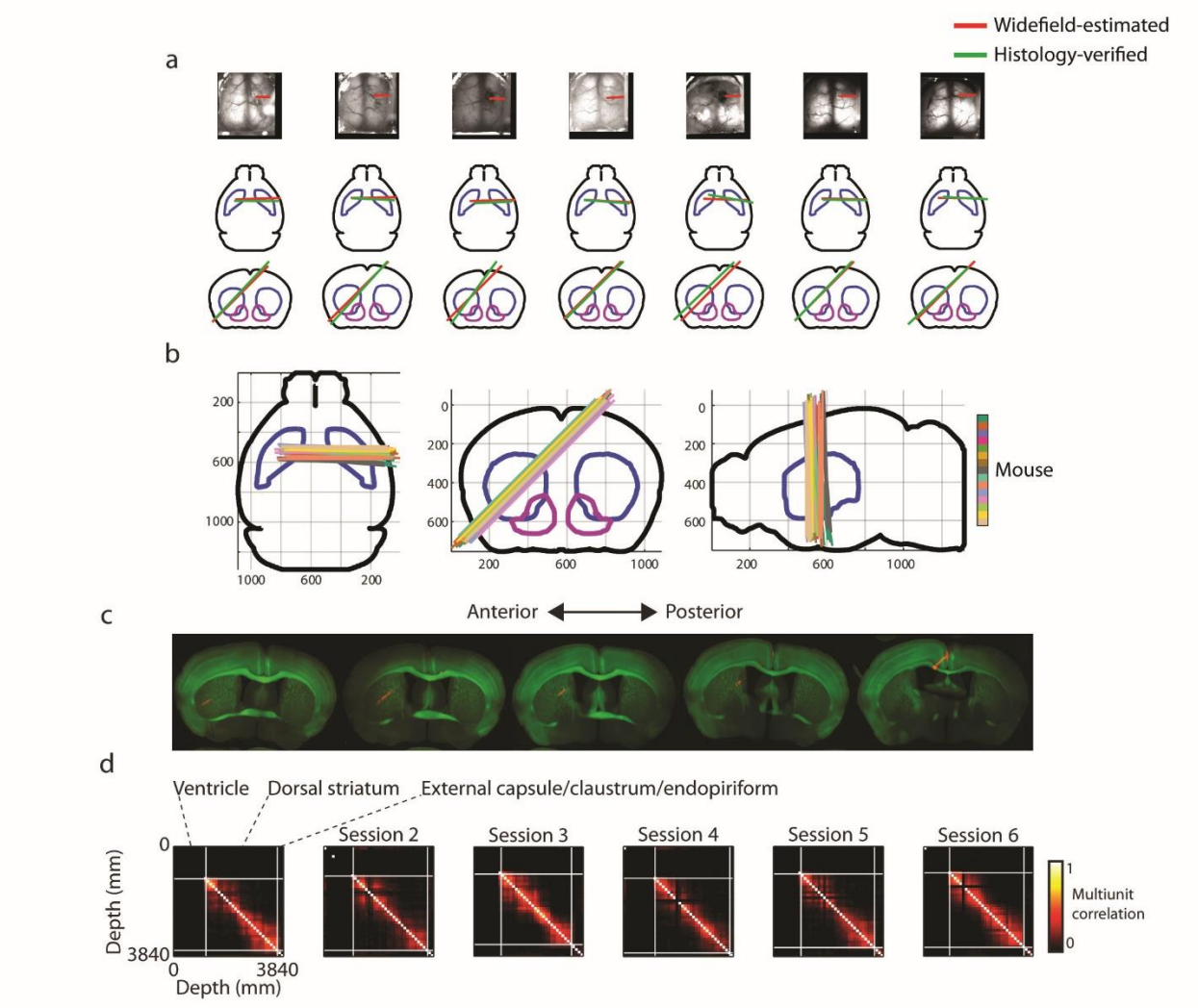

Extended Data Figure 3 | Striatal recording locations and electrophysiological borders. a, Top, widefield images used to approximate probe location (red line); middle/bottom, horizontal and coronal views of the brain with widefield-estimated probe location (red line) and histologically verified probe location (green line). Black outline, brain; blue outline; dorsal striatum, purple outline; ventral striatum. Widefield-estimated probe locations closely match histologically verified probe locations. **b,** Widefield-estimated probe location of all trained mice plotted in Allen CCF coordinates. **c,** Example histology showing GCaMP6s fluorescence (green) and dye from the probe (red). **d,** Example multiunit correlation matrix by depth along the probe for multiple sessions in the mouse from (c), with the borders of the striatum approximated medially by the lack of spikes in the ventricle and laterally by the sudden drop in local multiunit correlation. Dye from (c) corresponds to session 1 in (d) and histology-validated regions are labeled.

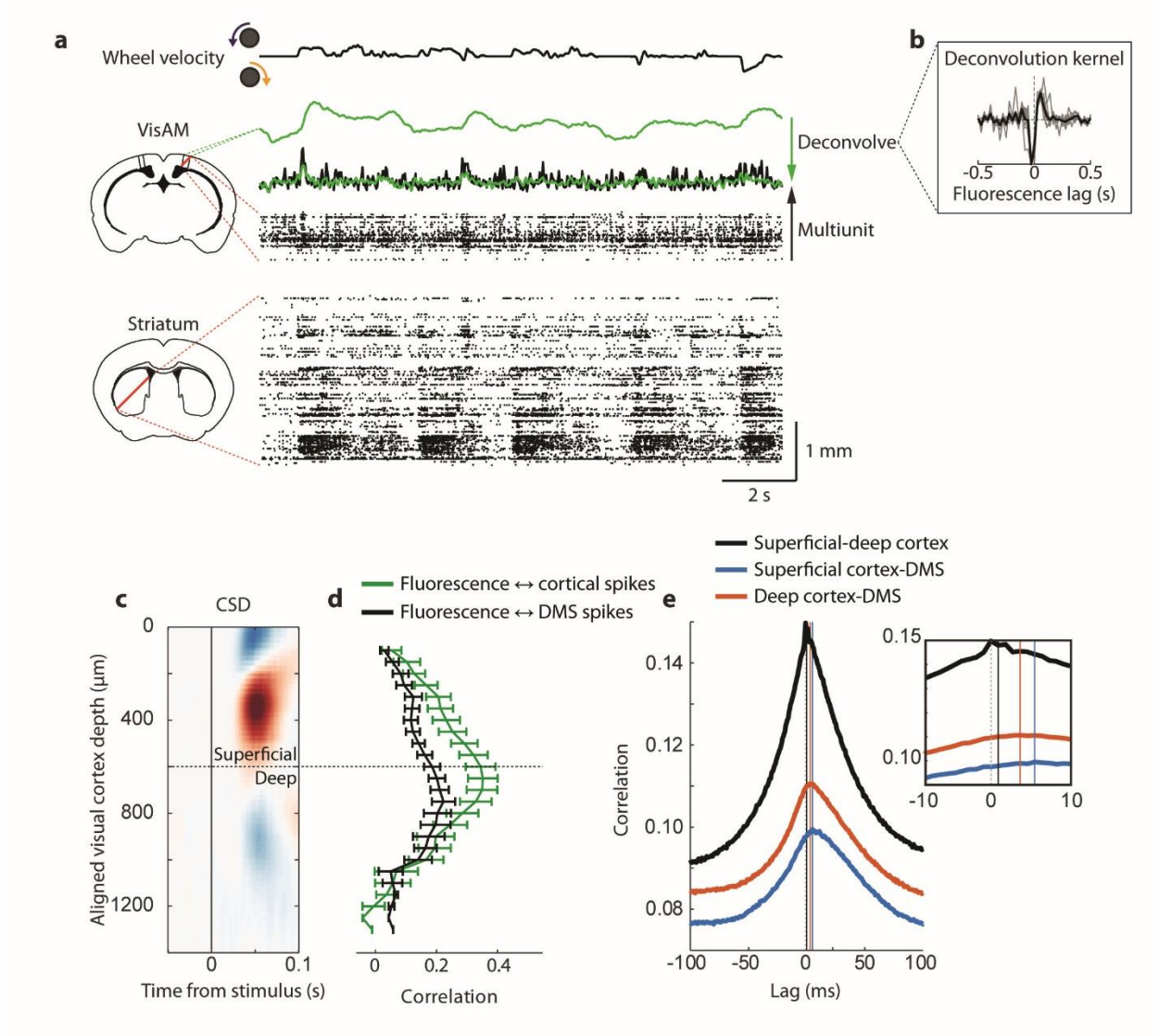

Extended Data Figure 4 | Relationship of cortical spiking with cortical fluorescence and with striatal spiking. a, Example triple recording with widefield imaging, VISam electrophysiology, and striatal electrophysiology during behavior. **b,** Deconvolution kernel obtained by predicting cortical multiunit spikes from cortical fluorescence around the probe (black, mean; gray, individual sessions). **c,** Current source density (CSD) from average stimulus responses aligned and averaged across sessions used to identify superficial and deep cortical layers. Horizontal dashed line represents the estimated border between superficial and deep layers. **d,** Correlation of VISam spiking with deconvolved fluorescence (green) and dorsomedial striatal spiking (black) (mean ± s.e.m. across sessions). Cortical fluorescence and striatal spiking are both correlated with deep-layer spiking with a similar laminar profile (correlation between fluorescence and striatal depth profiles compared to depth-shifted distribution, r = 0.57 ± 0.14 mean ± s.e.m. across 10 sessions, $p = 9.0*10^{-4}$). **e,** Cross-correlation of multiunit activity across superficial cortex, deep cortex, and the dorsomedial striatum. Deep cortical spiking leads striatal spiking by ~3ms.

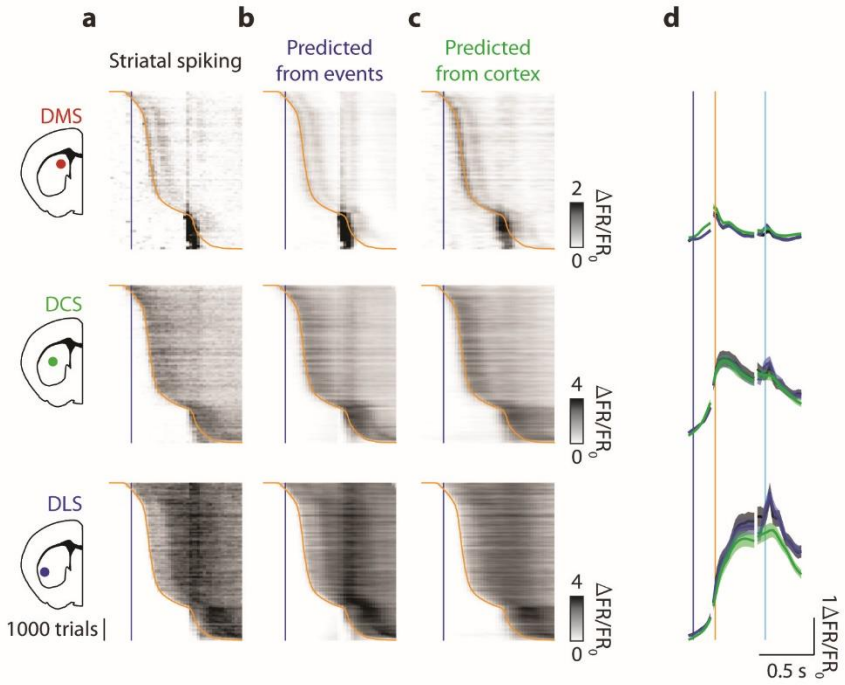

Extended Data Figure 5 | Striatal activity during trials with ipsilateral stimuli and ipsilaterally-orienting movements. a, Activity for each striatal domain across all trials from all sessions with ipsilateral stimuli, ipsilaterally-orienting movements, and rewards, plotted as in **Fig. 3a**. Trials are sorted vertically by reaction time; blue line: stimulus onset, orange curve: movement onset. Activity within each timepoint is smoothed with a running average of 100 trials to display across-trial trends. **b,** Prediction of activity in each striatal domain by summing kernels for task events displayed as in **Fig. 3c**. **c,** Prediction of striatal activity from cortical activity displayed as in **Fig. 3d**. **d,** Trial-averaged activity in each striatal domain (black), predicted from task events (blue), and predicted from cortical activity (green), aligned to stimulus (blue line), movement (orange line), and reward (cyan line) (mean ± s.e.m across sessions). Plotted as in **Fig. 3e.**

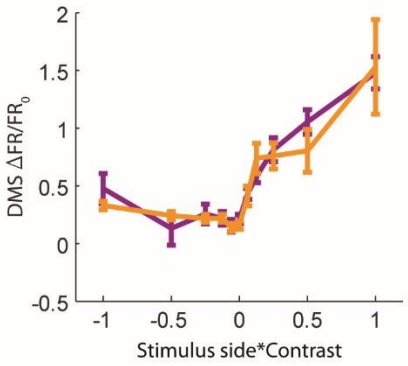

Extended Data Figure 6 | Visual responses in dorsomedial striatum do not depend on upcoming movement choice. Curves show average stimulus response (0-0.2 s after stimulus onset) in the dorsomedial striatum, as a function of contrast and side (left-hand stimuli are negative, right-hand stimuli are positive), for trials with contralateral-orienting (purple) and ipsilateral-orienting (orange) movements (mean ± s.e.m. across sessions). Movement choice does not affect stimulus responses, indicating that stimulus responses are purely sensory, rather than linked to decisions (2-way ANOVA on stimulus and choice, interaction effect: $p = 0.56$ for 77 sessions).

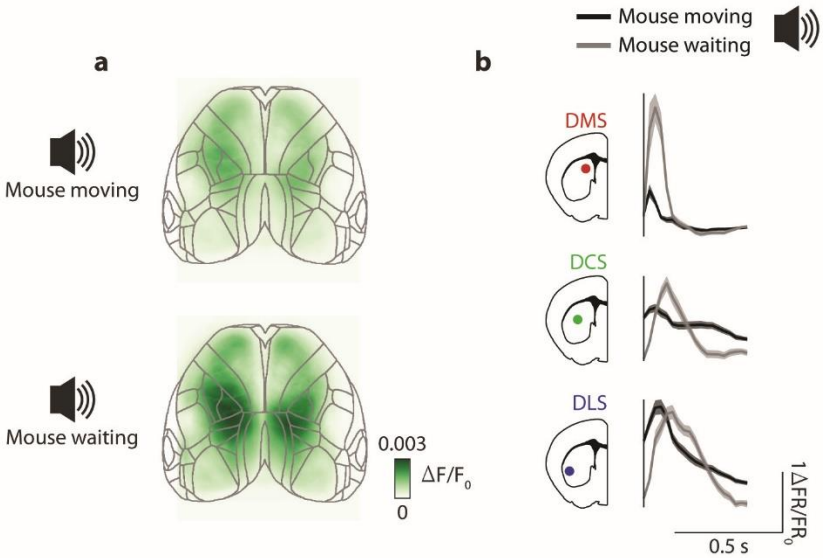

Extended Data Figure 7 | Responses to the auditory Go cue are suppressed by ongoing movement. a, Go cue kernel (lag = 50 ms after Go cue shown) obtained when predicting cortical activity from task events, for trials with movement onset before the Go cue (top) and after the Go cue (bottom). **b,** Go cue kernel obtained when predicting activity in each striatal domain from task events (as in Fig. 3b), for trials with movement onset before the Go cue (black) and after the Go cue (gray). Note that responses to the Go cue are much larger in parietal cortex and DMS when the mouse is not moving.

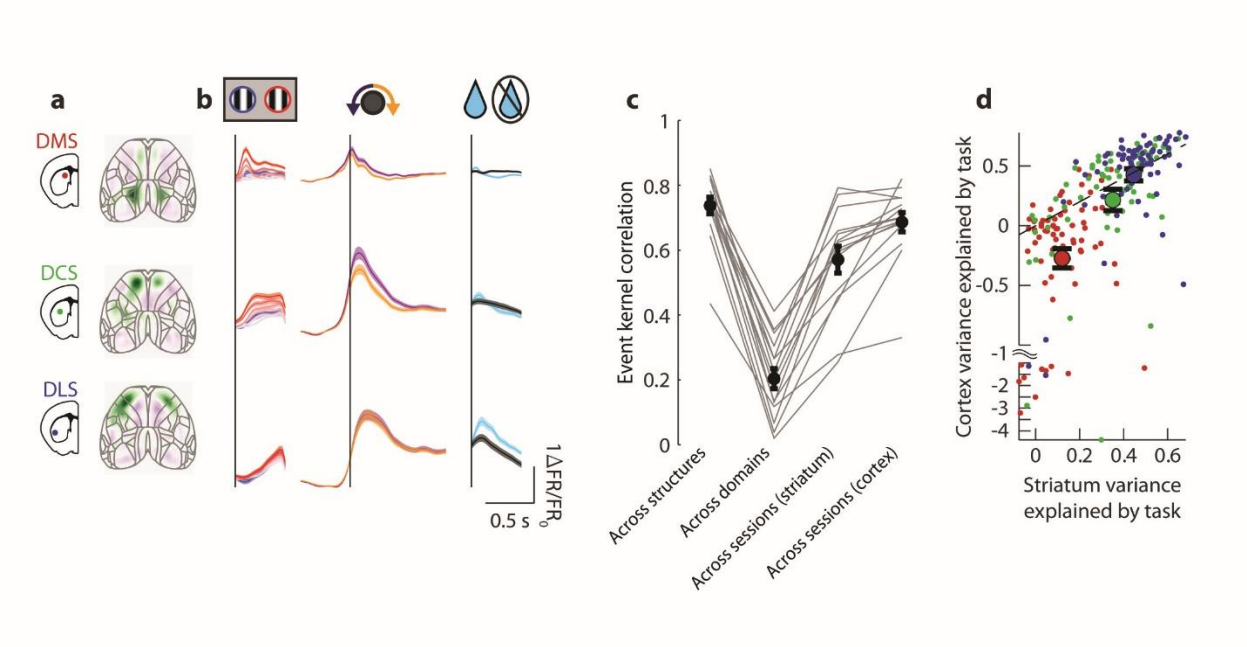

Extended Data Figure 8 | Task kernels for cortical activity associated with each striatal domain match task kernels for striatal activity. a, Maps of the cortical regions associated with each striatal domain. **b**, Temporal kernels obtained when predicting activity in these three cortical regions from task events for stimuli (left), movements (middle), and outcome (right) (mean ± s.e.m across sessions), plotted as in **Fig. 3b**. **c,** Correlation of task kernels for striatal and cortical activity. Columns from left to right: correlation of striatal kernels with topographically-aligned cortical kernels, within the same session; correlation of striatal kernels for different domains within the same session; correlation of striatal kernels from different sessions but the same striatal domain, and correlation of cortical kernels obtained from different sessions, but for cortical regions related to striatal domain. Gray lines show single sessions; black points and error bars show mean ± s.e.m across mice. The kernels obtained for topographically aligned striatal domains and cortical regions are more correlated than kernels for different striatal domains (signed-rank test, $p = 6.1*10^{-5}$ for 15 mice), indicating task kernels are domain-specific and shared between associated cortical and striatal regions. Correlations are also higher between matched striatal and cortical activity within-sessions, than between kernels fit to the same striatal domain on different sessions (signed-rank test, $p = 1.2*10^{-4}$), indicating that differences between cortical and striatal task responses are smaller than session-to-session variability. **c,** Cross-validated fraction of striatal variance predicted by task events vs. fraction of variance in the associated cortical regions predicted from task events. Small dots, individual sessions (three points plotted for each session, color coded by striatal domain); large dots, mean ± s.e.m across sessions. The task is an equal or worse predictor of cortical activity compared to striatal activity, indicating that the task responses are not more consistent within the cortex compared to the striatum (signed-rank test, DMS p = 5.8*10-8, DCS p = 0.88, DLS p = 0.02 across 77 sessions).

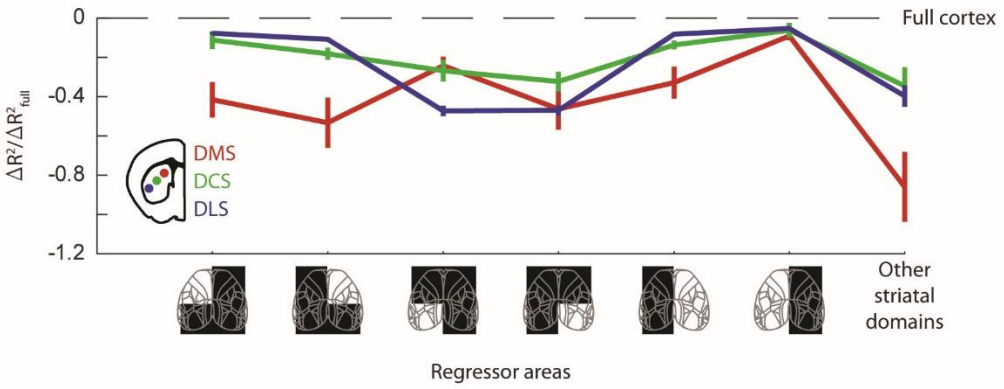

Extended Data Figure 9| Prediction of striatal activity from subregions of cortex, and from other striatal domains. We predicted activity in each striatal domain from subregions of cortex (indicated by white regions in diagrams below x-axis) or from the other two striatal domains (far right). Each curve shows the relative cross-validated fraction of explained variance $((R^2_{region} - R^2_{full\ cortex}) / R^2_{full\ cortex})$ for the color-coded striatal domain. Error bars represent s.e.m. across sessions. Predictions are best from the associated cortical regions (2-way ANOVA on session and cortical subregion, subregion effect: $p_{DMS} = 4.6*10^{-3}$, $p_{DCS} = 4.8*10^{-5}$, $p_{DLS} = 3.1*10^{-85}$ across 77 sessions) and striatal activity is less well predicted from other striatal domains than from cortex (signed-rank test, $p_{DMS} = 1.6*10^{-10}$, $p_{DCS} = 2.1*10^{-5}$, $p_{DLS} = 8.4*10^{-10}$ across 77 sessions).

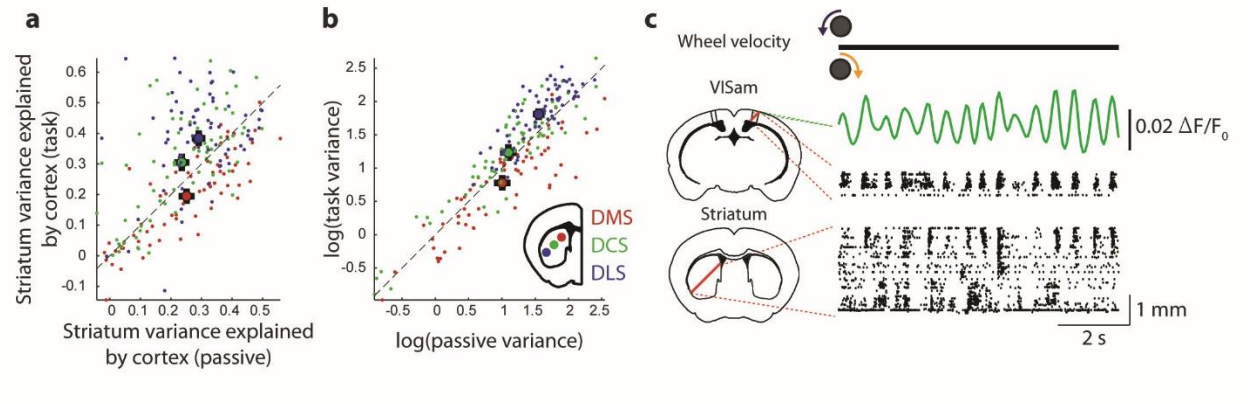

Extended Data Figure 10| Prediction of striatal from cortical activity during passive periods. a, Cross-validated fraction striatal variance predicted from cortex in task vs. passive states. Mice in the task state were performing the task, while mice in the passive state were viewing retinotopic mapping stimuli. Three small dots are plotted for each session, color coded according to striatal domain. Large dots: mean ± s.e.m across sessions. Dorsomedial striatum is predicted slightly better from cortex in the passive state, but dorsocentral and dorsolateral striatum is predicted slightly worse the passive state (signed-rank test, DMS $p = 6.2*10^{-7}$, DCS $p = 1.9*10^{-4}$, DLS $p = 1.6*10^{-5}$ across 77 sessions). **b,** Variance of striatal activity across behavioral and passive states. Small dots, sessions; large dots, mean ± s.e.m across sessions. During the passive state, the dorsomedial striatum exhibits more variance while the dorsomedial and dorsolateral striatum exhibit less variance (signed-rank test, DMS $p = 3.0*10^{-6}$, DCS $p = 1.3*10^{-4}$, DLS $p = 1.1*10^{-10}$ across 77 sessions), matching the differences in predictability between states. **c,** Example widefield, visual cortical electrophysiology, and striatal electrophysiology session in the passive state, showing coherent low-frequency oscillation in VISam and dorsomedial striatum (plotted as in **Extended Data Fig. 4a**, from the same session session).

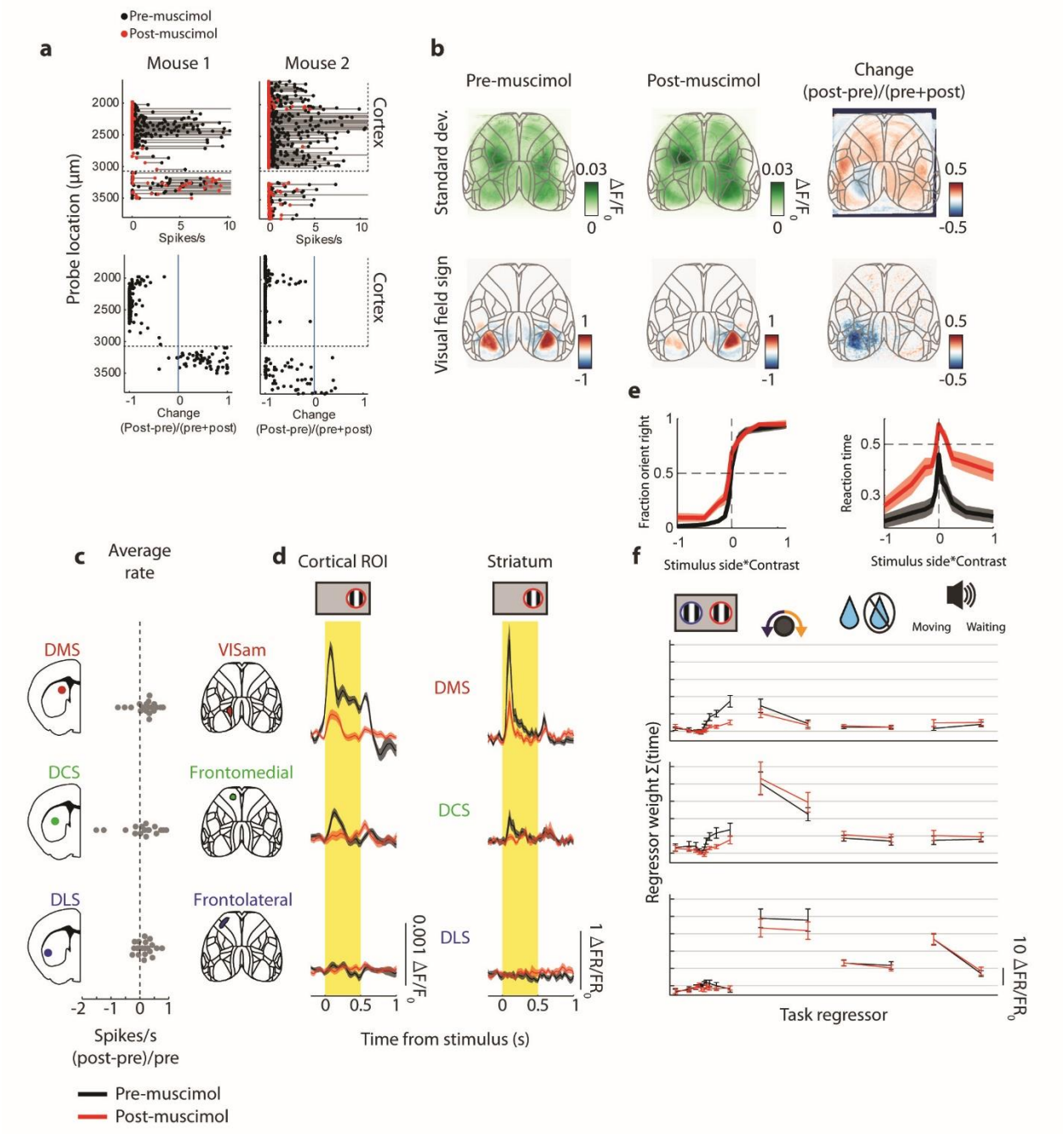

Extended Data Figure 11 | Visual cortical inactivation selectively eliminates striatal visual responses. a, Spike-sorted cortical unit firing rates by depth before (black) and after (red) topical muscimol application. Horizontal dotted line indicates bottom edge of cortex. Topical muscimol effectively silences the full cortical depth. **b,** Cortical fluorescence standard deviation (top) and retinotopic visual field sign (bottom) before and after muscimol application. Muscimol was centered on visual area AM and spread laterally to other visual areas. **c,** Average relative firing rate change in each striatal domain before and after cortical inactivation. Firing rate increases slightly after cortical inactivation (signed-rank test, DMS $p = 0.04$, DCS $p = 0.02$, DLS $p = 0.02$ across 22 sessions). **d,** Passive responses to visual stimuli in cortical ROIs (left) and striatal domains (right) before (black) and

479 after (red) inactivation of visual cortex. Muscimol proportionally reduced the stimulus response in VISam and dorsomedial
480 striatum (correlation between fractional reduction of each area: $r = 0.48$, $p = 0.04$ across 22 sessions). **e,** Psychometric curve
481 (left) and median reaction (right) as a function of stimulus contrast and side as in **Extended Data Fig. 1b**, before (black) and
482 after (red) muscimol in visual cortex (mean ± s.e.m across sessions). Task performance becomes worse for stimuli contralateral
483 to the muscimol (2-way ANOVA on stimulus and condition, interaction effect: $p = 0.04$ across 22 sessions) and reaction times
484 become longer across stimuli (2-way ANOVA on stimulus and condition, condition effect: $p = 1.1*10^{-26}$ across 22 sessions). **f,**
485 Kernels predicting striatal activity from task events to striatal activity before (black) and after (red) visual cortical muscimol
486 (mean ± s.e.m across sessions). Stimulus kernel weights decrease after muscimol while other kernel weights do not change
487 significantly (2-way ANOVA on regressor and condition, condition effect on stimuli regressors: DMS $p = 2.0*10^{-7}$, DCS $p =$
488 $8.4*10^{-6}$, DLS $p = 0.03$, $p > 0.05$ for other domains and regressors across 22 sessions).

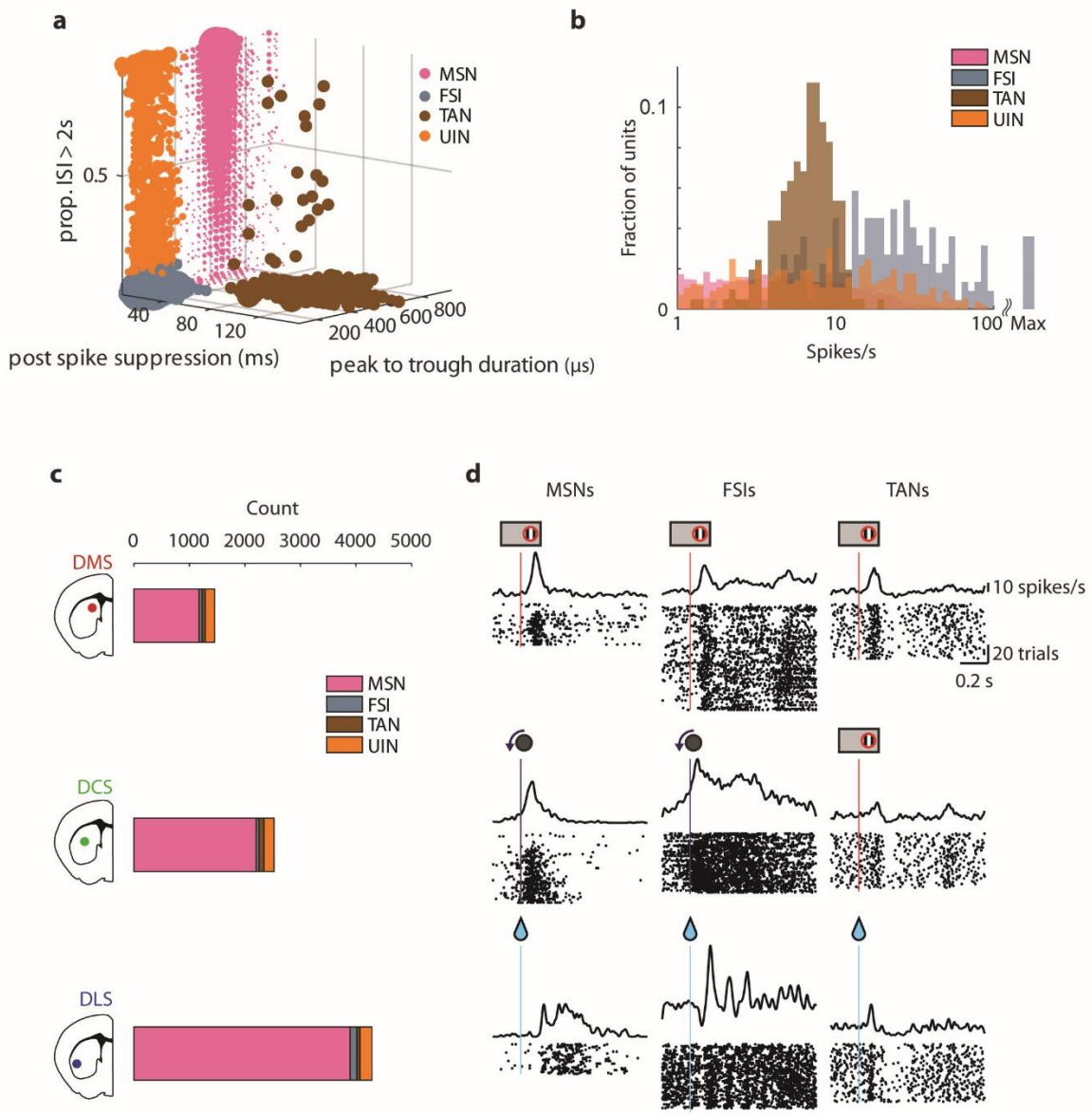

Extended Data Figure 12| Identifying striatal cell types with electrophysiology. a, Striatal cells were identified as medium spiny neurons (MSNs), fast-spiking interneurons (FSIs), tonically-active neurons (TANs) and a fourth class of "unidentified interneurons" (UINs, not analyzed further), according to waveform duration, length of post-spike suppression, and fraction of long ISIs (see Methods). **b,** Histogram of firing rates across all units within each cell type. **c,** Number of units classified in each domain as belonging to each cell type. **d,** Raster plots for one example cell of each type in each domain, aligned to the indicated event. Top row: dorsomedial striatum; middle row, dorsocentral striatum; bottom row, dorsolateral striatum.

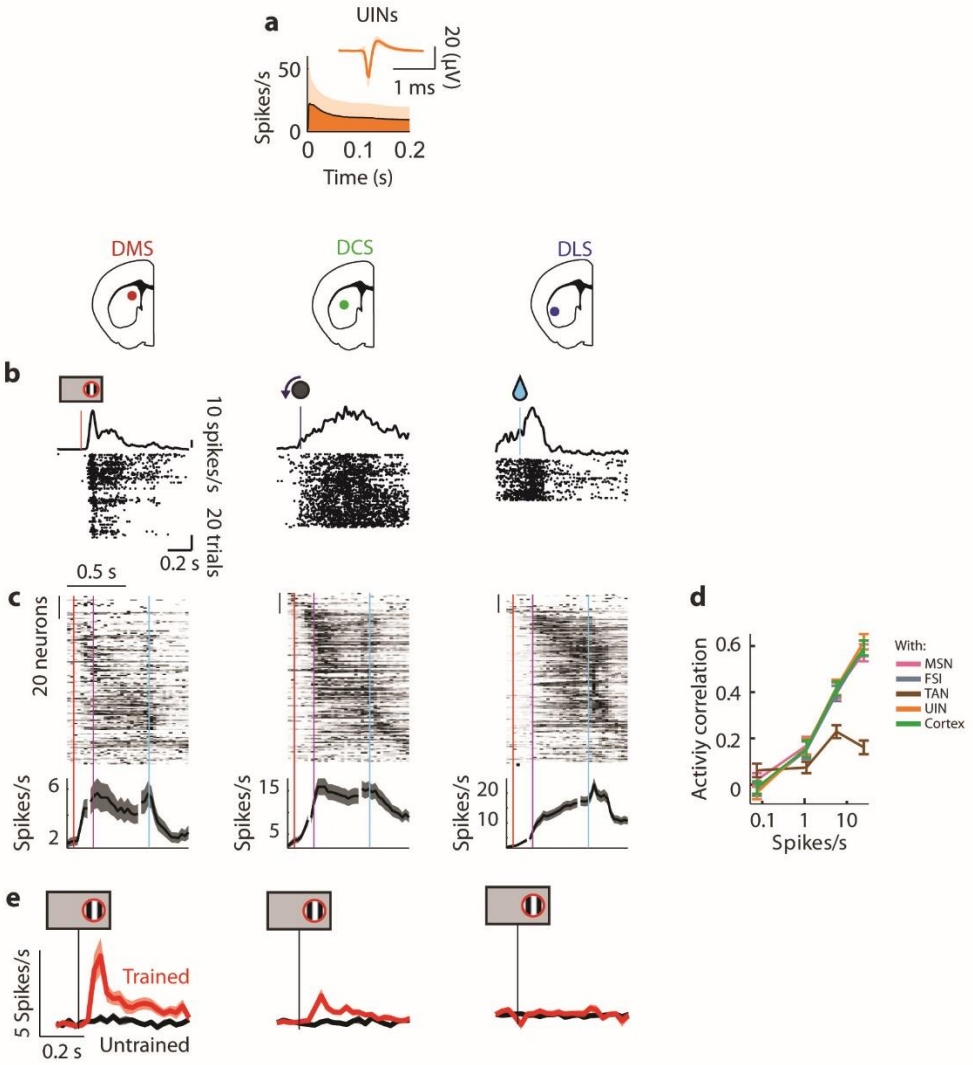

Extended Data Figure 13 | Striatal unidentified interneuron (UINs) activity. a, Waveform and autocorrelelogram used to define striatal cells as unidentified interneurons (UINs) (mean ± s.t.d. across cells). **b,** Example raster plots for UINs in each domain. **c,** Heatmaps, spiking in individual cells aligned to contralateral stimuli (left), contralaterally-orienting movements (middle), and rewards (right), averaged across trials with reaction times less than 500 ms, max-normalized, and sorted by time of maximum activity using half of the trials and plotting the other half of trials (as in Fig. 4b). Line plots, average activity across neurons (as in Fig. 4c). **d,** Correlation of the activity of each neuron as in (c) with the average activity within cell types or cortical activity from an ROI corresponding to each domain (calculated from non-overlapping sessions to account for interneuron sparsity and binned by firing rate of the neuron) (mean ± s.e.m. across sessions). UINs were equally correlated to other UINs, MSNs, FSIs, and cortical activity (2-way ANOVA on firing rate and type, type effect: $p = 0.56$ across 77 sessions) and uncorrelated to TAN activity (2-way ANOVA on firing rate and type, type effect: $p = 2.7*10^{-12}$ across 77 sessions). **e,** Activity during passive stimulus presentations in untrained (black) and trained (red) mice (mean ± s.e.m across recordings), activity increases in the DMS and DCS (average activity 0-0.2 s rank-sum test, DMS: $p = 5.5*10^{-4}$, DCS: $p = 1.4*10^{-4}$ across 77 sessions).

Methods

All experiments were conducted according to the UK Animals (Scientific Procedures) Act 1986 under personal and project licenses issued by the Home Office.

Animals

Mice were adult (6 weeks or older) male and female transgenic mice (TetO-G6s;Camk2a-tTa, Ref. [1]) which did not show evidence of epileptiform activity[2].

Surgery

Two surgeries were performed for each animal, the first for headplate implantation and widefield imaging preparation, and the second for a craniotomy for acute electrophysiology. Mice were anesthetized with isoflurane, injected subcutaneously with Carprieve, and placed in a stereotaxic apparatus on a heat pad. The head was then shaved, the scalp cleaned with iodine and alcohol, and the scalp was removed to expose the skull. The cut skin was sealed with (VetBond, World Precision Instruments), the skull was scraped clean and a custom headplate was fixed to the interparietal bone with dental cement (Super-Bond C&B). A plastic 3D-printed U-shaped well was then cemented to enclose the edges of the exposed skull. A thin layer of VetBond was applied to the skull followed by two layers of UV-curing optical glue (Norland Optical Adhesives #81, Norland Products). Carprieve was added to the drinking water for 3 days after surgery. For electrophysiological recordings, on the first day of recording mice were anesthetized and a 1mm craniotomy was drilled or cut with biopsy punch approximately 200 µm anterior and 1000 µm lateral to bregma. The craniotomy was then covered with Kwik-Cast (WPI) and mice were given hours to recover before recording. Craniotomies were covered with Kwik-Cast between days.

Visually guided wheel-turning task

The task is described in detail elsewhere[3]. It was programmed in Signals, part of the Rigbox MATLAB package[4]. Mice were trained on a 2-alternative forced choice task requiring directional forelimb movements to visual stimuli (**Fig. 1**, **Extended Data Fig. 1a**). Mice were headfixed and rested their body and hind paws on a stable platform and their forepaws on a wheel that was rotatable to the left and right. Trials began with 0.5 s of enforced quiescence, where any wheel movements reset the time. A static vertical grating stimulus then appeared 90° from center with a gaussian window $\sigma = 20°$, spatial frequency 1/15 cycles/degree, and grating phase randomly selected on each trial. After 0.5 s from stimulus onset, a go cue tone (12 kHz, 100 ms) sounded and the position of the stimulus became yoked to the wheel position (e.g. leftward turns moved the stimulus leftward). Mice usually began turning the wheel before the go cue event on trials with 0% contrast (invisible) stimuli (**Extended Data Fig. 1c**), indicating a rapid decision process and expected stimulus time, although as the session progressed and mice became sated they began waiting for the go cue more often (**Extended Data Fig. 1d**). Bringing the stimulus to the center (correct response) locked the stimulus in the center for 1 s and 2 µL of water was delivered from a water spout near the mouse's mouth, after which the stimulus disappeared and the trial ended. Alternately, moving the stimulus 90° outward (incorrect response) locked the stimulus in place off-screen and a low burst of white noise played for 2 s, after which the trial ended. The stimulus contrast varied across trials taking the values of 0%, 6%, 12.5%, 25%, 50%, or 100%. Difficulty was modulated with an alternating staircase design, where even trials used a random contrast, and odd trials

546 followed a staircase that moved to a lower contrast after 3 correct responses and moved to higher
547 contrast after 1 incorrect response. Correct responses on high-contrast trials were encouraged by
548 immediately repeating all incorrect trials with 50% or 100% contrast, but these repeated trials were
549 excluded from all analyses. Other than repeat trials, stimulus side was selected randomly on each trial.
550 Mice were trained in stages, where first they were trained to ~70% performance with only 100%
551 contrast trials, then lower contrasts were progressively and automatically added as performance
552 increased. Imaging sessions began after all contrasts had been added, and simultaneous imaging and
553 electrophysiology sessions began after ~4 days of imaging-only sessions.

554 Widefield imaging and fluorescence processing

555 Widefield imaging was conducted with a sCMOS camera (PCO Edge 5.5) affixed to a macroscope
556 (Scimedia THT-FLSP) with a 1.0x condenser lens and 0.63x objective lens (Leica). Images were collected
557 with Camware 4 (PCO) and binned in 2x2 blocks giving a spatial resolution of 20.6 µm/pixel at 70 Hz.
558 Illumination was generated using a Cairn OptoLED with alternating blue (470 nm, excitation filter
559 ET470/40x) and violet (405 nm, excitation filter ET405/20x) light to capture GCaMP calcium-dependent
560 fluorescence and calcium-invariant hemodynamic occlusion respectively at 35 Hz per light source.
561 Illumination and camera exposure were triggered externally (PCIe-6323, National Instruments) to be on
562 for 6.5 ms including a 1 ms illumination ramp up and down time to reduce light-induced artifacts on the
563 Neuropixels probe. Excitation light was sent through the objective with a 3mm core liquid light guide
564 and dichroic (387/11 single-band bandpass) and emitted light was filtered (525/50-55) before the
565 camera.

566 To reduce data size for storage and ease of computation, widefield data was compressed using singular
567 value decomposition (SVD) of the form $\mathbf{F} = \mathbf{USV}^{\mathrm{T}}$**.** The input to the SVD algorithm was $\mathbf{F}$**,** the
568 $pixels \times time$ matrix of fluorescence values input to the SVD algorithm; the outputs were $\mathbf{U}$**,** the
569 $pixels \times components$ matrix of template images; $\mathbf{V}$ the $time \times components$ matrix of component
570 time courses; and $\boldsymbol{S}$ the diagonal matrix of singular values. The top 2000 components were retained,
571 and all orthogonally-invariant operations (such as deconvolution, event-triggered averaging and ridge
572 regression to predict striatal activity from the widefield signal) were carried out directly on the matrix $\mathbf{V}$,
573 allowing a substantial saving of time and memory.

574 Hemodynamic effects on fluorescence were removed by regressing out the calcium-independent signal
575 obtained with violet illumination from the calcium-dependent signal obtained with blue illumination. To
576 do this, both signals were bandpass filtered in the range 7-13 Hz (heartbeat frequency, expected to have
577 the largest hemodynamic effect), downsampling the spatial components 3-fold, and reconstructing the
578 fluorescence for each downsampled pixel. Pixel traces for blue illumination were then temporally
579 resampled to be concurrent with violet illumination (since colors were alternated), and a scaling factor
580 was fit across colors for each pixel. The scaled violet traces were then subtracted from the blue traces.

581 To correct for slow drift, hemodynamic-corrected fluorescence was then linearly detrended, high-pass
582 filtered over 0.01 Hz, and $\Delta F/F_0$ normalized by dividing by the average fluorescence at each pixel
583 softened by adding the median average fluorescence across pixels.

584 Widefield images across days for each mouse were aligned by rigid registration of each day's average
585 violet-illumination image which was dominated by vasculature (**Extended Data Fig. 2a**). Widefield
586 images across mice were aligned by affine alignment of average visual field sign maps for each mouse
587 (**Extended Data Fig. 2b-c**). The Allen Common Coordinate Framework (CCF v.3[5], © Allen Institute for

Brain Science) atlas was aligned to the grand average and symmetrized sign map across mice by assigning expected visual field sign to visual areas[6] and affine aligning the annotated CCF to the average sign map (**Extended Data Fig 2d**). Even though CCF alignment was done using posterior visual areas, it was successful in aligning the entire brain as evidenced by correspondence between correlated widefield regions and CCF borders (**Extended Data Fig. 2e-f**) and the ability to accurately estimate anterior probe trajectories from widefield images (**Extended Data Fig. 3a**).

To combine SVD-compressed widefield data across recordings, data was recast from experiment-specific SVD components into a master SVD basis set. These master SVD components were created by aligning and concatenating components $\mathbf{U}$ from the last imaging-only session of all animals (i.e. no craniotomy), performing an SVD on that concatenated matrix, and retaining the top 2000 components to serve as the master SVD component set. Temporal components ($\mathbf{S} * \mathbf{V}$) for each experiment were recast by

$$\mathbf{S} * \mathbf{V}_{master} = \mathbf{U}_{master}^{T} * \mathbf{U}_{experiment} * \mathbf{S} * \mathbf{V}_{experiment}$$

Fluorescence was deconvolved using a kernel fit from predicting cortical multiunit activity from widefield GCaMP6s fluorescence. This kernel was estimated using data from simultaneous widefield imaging and Neuropixels recordings in the visual cortex (**Extended Data Fig. 4a-b**, with the final deconvolution kernel being a mean of max-normalized kernels across recordings divided by the squared sum of weights across time. The deconvolution kernel was biphasic and roughly similar to a derivative filter (-1,1) (**Extended Data Fig. 4b**), consistent with rises in the GCaMP signal correspond to periods of spiking.

Neuropixels recordings

Electrophysiological recordings were made with Neuropixels Phase 3A probes[7] affixed to metal rods and moved with micromanipulators (Sensapex). Raw data within the action potential band (soft high-pass filtered over 300 Hz) was de-noised by common mode rejection (i.e. subtracting the median across all channels), and spike-sorted using Kilosort 2 (www.github.com/MouseLand/Kilosort2). Units representing noise were manually removed using phy[8]. Multiunit activity was then defined as spikes pooled from all Kilosort-identified units within a given segment of the probe.

Electrophysiological recordings were synchronized to widefield data and task events by aligning to a common digital signal randomly flipping between high and low states (produced from an Arduino) accounting for both clock offset and drift.

Light from the LED used during widefield imaging produced a substantial artifact in the electrophysiological data. This artifact was reduced by ramping the light over 1ms, and was removed from the action potential band by subtracting the average signal across all channels. Kilosort occasionally identified units from a small remaining artifact which were readily identifiable from their shape and regularity and were discarded. The light artifact was removed from the LFP band by subtracting a rolling median light-triggered average for each LED color.

Probe trajectories were reconstructed from histology (**Extended Data Fig. 3a**) using publicly available custom code (https://github.com/petersaj/histology). Probe trajectories were estimated from widefield images (**Extended Data Fig. 3b**) by manually identifying the probe in the image and transforming the location into CCF coordinates using the retinotopy-CCF alignment for that recording.

Striatal electrophysiology and depth-alignment

For striatal recordings, probes were inserted at approximately 200 µm anterior and 1000 µm lateral to bregma at a 45° angle from horizontal (diagonally downwards) and 90° from the anterior-posterior axis (straight coronally) to a depth of ~6 mm from the cortical surface to reach the contralateral striatum. Electrophysiological data was recorded with Open Ephys[9].

The borders of the striatum were identified within each recording using the ventricle and dorsolaterally-neighboring structure (likely the endopiriform nucleus) as electrophysiological landmarks. Since no units were detected in the ventricle, the start of the striatum on the probe was marked as the first unit after at least a 200 µm gap from the last unit (or the top of the probe if no cortical units were detected). Detected units were continuous after the ventricle, but multiunit correlation in temporal bins of 10 ms and sliding spatial bins of 100 µm revealed a sharp border in correlation at a location consistent with the end of the striatum (**Extended Data Fig. 3d**). This border was present in every recording; we used to define the end of the striatum on the probe.

Striatal recordings were aligned by depth using the lateral striatal border, as the lateral border was sharp while the medial border was inferred from lack of units and therefore imprecise. The location of striatal units was then defined as distance from the lateral border, and depth-aligned analyses were performed on these distances divided into ~200 µm segments (**Fig. 1e, Fig. 2a-b**). Only depths present in > 50% of recordings are shown, eliminating a sparse subset of medial depths in recordings with an unusually large segment of the probe corresponding to the striatum. Note that aligning by depth is only approximate, while aligning by functionally associated cortical maps provides a much more precise method of alignment (below).

Single-unit analysis and striatal cell-type classification

High-quality single units were defined by the following criteria:

1. Waveform trough to peak amplitude of more than 15 µV
2. Minimum of 300 spikes
3. Less than 30% of spikes missing, estimated by fitting a gaussian to the spike amplitude distribution with an additional cut-off parameter below which no spikes are present (using the python function scipy.optimize.curve_fit)
4. Waveform trough that preceded a waveform peak, to eliminate axonal spikes[10].
5. An estimated false-positive rate of less than 10% using the approach of Ref. [11]. This estimates the false-positive rate F_p as the solution to

$$r = 2(\tau_R - \tau_C)N^2\left(1 - F_p\right)F_p/T$$

Where r is the number of refractory period violations; τ_R the refractory period (taken as 2 ms), τ_C the censored period (taken as 0.5 ms), τ_C the number of spikes, F_p the false positive rate, T the total recording time. MATLAB's built-in function roots was used for this. If an imaginary number was returned by the function, due to r being too high, the F_p rate was set to 1 as in Ref. [11], and the unit rejected.

Units passing these quality criteria were then classified into four putative striatal cell types: medium spiny neurons (MSNs), fast-spiking interneurons (FSIs), tonically-active neurons (TANs) and a fourth class of unidentified interneurons (UINs) (**Extended data Figs. 12, 13**). Neurons with narrow waveforms (trough to peak waveform duration <= 400 µs) were identified as either FSIs or UINs as in Ref. [12]. Putative FSIs and UINs were then separated using the proportion of time associated with long interspike-intervals (ISIs >2 s) by summing ISIs longer than 2 s and dividing the sum by the total recording time (as calculated in Ref. [13]): Neurons where this ratio was more than 10% were classified as UINs, and the others as FSIs. The remaining units were presumed to be TANs and MSNs, which were further separated using the post-spike suppression. We measured the length of time that a unit's firing rate was suppressed following an action potential by counting the number of 1ms bins in its autocorrelation function until the unit's firing rate was equal or greater to its average firing rate over the 600 ms to 900 ms autocorrelation bins. Units with post-spike suppression of > 40 ms were labelled TANs, and the remaining units were labelled MSNs. A few units had short waveforms (< 400 µs) and long post-spike suppression (> 40 ms). These units were very rare (36/8,303) and exhibited TAN-like responses and might therefore possibly be TAN neurites; they were excluded from further analysis.

Cortical electrophysiology and alignment

For cortical recordings, a second craniotomy was performed over VISam targeted by retinotopic visual field sign maps relative to vasculature. During recording, a second Neuropixels probe was inserted into VISam at a 45° angle from horizontal (diagonally downwards) and 90° from the anterior-posterior axis (straight coronally) to a depth of ~2 mm from the cortical surface.

Cortical depth was aligned across recordings using current source density (CSD) analysis. Mice were passively presented with visual gratings, and the CSD was computed as the second spatial derivative of the stimulus-triggered average LFP signal, smoothed by a boxcar rolling average of 10 channels. The average CSD 40-60 ms after the stimulus was then aligned across recordings by interpolation using the maximum sink (**Extended Data Fig. 4c**, red patch) and the first source (**Extended Data Fig. 4c**, top blue patch). The "aligned visual cortex depth" (**Extended Data Fig. 4c**) was then set relative to these points, with the first source being 0 and the maximum sink being the median source-sink distance across sessions. Superficial and deep layers were defined as being above or below midway from the sink to the lower source (**Extended Data Fig. 4c,** horizontal line). The ventral border of the cortex was made clear by a gap in detected units corresponding to the white matter.

Regression from task events to activity

Regression from task events to striatal multiunit activity or deconvolved cortical fluorescence activity using linear regression of the form

$$\begin{pmatrix} F_{t1} \\ \vdots \\ F_{tn} \end{pmatrix} \sim \begin{pmatrix} Task\ event_{event\ 1, time\ lag\ 1, t\ 1} & \cdots & Task\ event_{event\ n, time\ lag\ n, timepoint\ 1} \\ \vdots & \ddots & \vdots \\ Task\ event_{event\ 1, time\ lag\ 1, tn} & \cdots & Task\ event_{event\ n, time\ lag\ n, timepoint\ n} \end{pmatrix} * K_{task \to activity}$$

Here, $K_{task \to activity}$ represents a vector containing the concatenated estimated kernels for each event type, estimated by least squares using MATLAB's \ operator. F_{t1} to F_{tn} represent the fluorescence or firing rate time course to be predicted, "baseline-subtracted" by subtracting the average activity 0.5-0 s before stimulus onset, during which time the animals were required not to turn the wheel. For each

event type, a task matrix was constructed as a sparse Toeplitz matrix with a diagonal series of 1 s for each event at each time lag, with zeros elsewhere. Toeplitz matrices were made for each event type: stimulus onset (one for each stimulus side*contrast, lags of 0-0.5 s), movement onset (one each for left and right final response, lags of -0.5-1 s), go cue onset (one for trials where mice had already begun moving and one for trials with no movement before the go cue, lags of 0-0.5 s), and outcome (one for water and one for white noise, lags of 0-0.5 s). These matrices were horizontally concatenated to produce the matrix shown in the above equation. Regression was 5-fold cross-validated by splitting up timepoints into consecutive chunks.

Regression from cortical activity to striatal activity

Normalized, hemodynamically-corrected, and deconvolved widefield fluorescence was regressed to striatal multiunit activity using ridge regression. Regression took the form

$$\begin{pmatrix} F_{t1} \\ \vdots \\ F_{tn} \\ 0 \\ \vdots \\ 0 \\ 0 \end{pmatrix} \sim \begin{pmatrix} SV_{component\ 1,time\ lag\ 1,timepoint\ 1} & \cdots & SV_{component\ n,time\ lag\ n,timepoint\ 1} & 1 \\ \vdots & \ddots & \vdots & \vdots \\ SV_{component\ 1,time\ lag\ 1,timepoint\ n} & \cdots & SV_{component\ n,time\ lag\ n,timepoint\ n} & 1 \\ \lambda & 0 & 0 & 0 \\ \vdots & \ddots & \vdots & \vdots \\ 0 & 0 & \lambda & \vdots \\ 0 & 0 & 0 & 0 \end{pmatrix} * K_{cortex \rightarrow striatum}$$

Here, F_{t1} to F_{tn} represent the standard-deviation-normalized striatal spiking time course to be predicted. $K_{cortex \rightarrow striatum}$ represents the estimated spatiotemporal kernel from cortical fluorescence to standard-deviation-normalized striatal spiking estimated by least squares using MATLAB's \ operator. To make the design matrix, a Topelitz matrix was constructed for each temporal SVD component of the cortical widefield, scaled by the singular values (S*V), staggered across a range of time values (-100 ms to +100 ms). These Toeplitz matrices were horizontally concatenated, also including a column of ones to allow an offset term. To regularize using ridge regression, this matrix was vertically concatenated above diagonal matrix of regularization values λ, and the striatal activity time courses F were concatenated above the same number of zeros. Regression was 5-fold cross-validated by splitting up timepoints into consecutive chunks, and values for λ were determined empirically for each experiment by regressing from cortical fluorescence to multiunit from the whole striatum across a range of λ values and finding the λ that yielded the largest cross-validated explained variance.

Striatal domain assignments

Striatal domains were defined from cortical maps as spatial kernels (time lag = 0) described above for consecutive 200 µm segments of the Neuropixels track through the striatum recorded in each experiment. The cortical maps were combined across all experiments and split into 3 groups through K-means, and the average cortical map for each group was used as a template for each striatal domain. The spatial map from each 200 µm striatal segment was then assigned to one group by highest correlation with the template maps. Striatal domain assignments were smoothed using a 3-segment median filter and restricted to a standard order by replacing mis-ordered assignments with their nearest neighbor. This process ensured contiguous domains and was empirically successful at removing aberrations. Our dorsomedial, dorosocentral, and dorsolateral domains approximately correspond to

the medial dorsomedial subdivision, lateral dorsomedial subdivision, and dorsolateral domains of Hunnicutt et al.[14] and the domains i.dm.d/dm/im, i.dm.cd/i.vl.cvl, and i.vl.v/vt in Hintiryan et al.[15].

Cortical regions-of-interest (ROIs) for striatal domains

Cortical regions of interest corresponding to the most correlated cortical region for each striatal domain (used in **Fig. 5a, Extended Data Fig. 10**) were generated using the template cortical map for each domain described above. Pixels were thresholded above 75% of the maximum weighted pixel and contralateral pixels or clusters smaller than 100 pixels were removed, resulting in a discrete cortical ROI over the region most correlated with each striatal domain.

Allen connectivity maps

Anatomical projections were labeled using the Allen connectivity database[16] (**Fig. 2h**). The Allen API (2015) was queried for injection sites within the cortex that yielded axon terminals in each striatal domain, and the seed points used for each striatal domain were the center-of-mass for each domain relative to the longest recorded striatal length and interpolated into the targeted striatal trajectory in the CCF atlas (shown in **Fig. 2d**). To maximize coverage across the brain since the Allen connectivity database has different left and right hemisphere injections, queries were performed for striatal sites bilaterally and results from the right striatum were mirrored and combined with the results from the left striatum. The cortical sites with striatal projections returned by the API were then plotted as a heatmap by binning across space and blurring with a Gaussian filter.

Muscimol experiments

For inactivation experiments, in the same surgery that placed a craniotomy with access to the striatum, a second craniotomy was performed over visual area AM targeted by retinotopic visual field sign maps relative to vasculature. During the experiment, mice performed the task for approximately half of the normal number of trials and were then shown retinotopic-mapping stimuli and passive gratings. Muscimol (Sigma, 5 mM in ACSF) was then applied topically by placing muscimol-soaked gelfoam in the visual area AM craniotomy for 40 minutes, with additional ACSF applied at 20 minutes to prevent drying. Mice then performed the task until they no longer engaged and were again shown retinotopic-mapping stimuli and passive gratings.

The effect of topical muscimol by cortical depth was assessed in two separate mice (**Extended Data Fig. 11a**) by inserting a Neuropixels probe near the edge of a craniotomy and recording activity before and after muscimol application.

In sessions with cortical inactivation, mice performed the task as described above without the inclusion of repeat trials for incorrect 50% and 100% contrast stimuli described above. This was normally included to discourage bias, and excluded in these sessions to allow for a muscimol-induced bias.

Methods references

1. Wekselblatt, J. B., Flister, E. D., Piscopo, D. M. & Niell, C. M. Large-scale imaging of cortical dynamics during sensory perception and behavior. *J. Neurophysiol.* **115,** 2852–2866 (2016).
2. Steinmetz, N. A., Buetfering, C., Lecoq, J., Lee, C. R., Peters, A. J., Jacobs, E. A. K., Coen, P., Ollerenshaw, D. R., Valley, M. T., de Vries, S. E. J., Garrett, M., Zhuang, J., Groblewski, P. A., Manavi, S., Miles, J., White, C., Lee, E., Griffin, F., Larkin, J. D., *et al.* Aberrant Cortical Activity in Multiple GCaMP6-Expressing Transgenic Mouse Lines. *Eneuro* **4,** ENEURO.0207-17.2017

(2017).

3. Burgess, C. P., Lak, A., Steinmetz, N. A., Zatka-Haas, P., Bai Reddy, C., Jacobs, E. A. K., Linden, J. F., Paton, J. J., Ranson, A., Schröder, S., Soares, S., Wells, M. J., Wool, L. E., Harris, K. D. & Carandini, M. High-Yield Methods for Accurate Two-Alternative Visual Psychophysics in Head-Fixed Mice. *Cell Rep.* **20,** 2513–2524 (2017).

4. Bhagat, J., Wells, M. J., Harris, K. D., Carandini, M. & Burgess, C. P. Rigbox: An Open-Source Toolbox for Probing Neurons and Behavior. *Eneuro* **7,** ENEURO.0406-19.2020 (2020).

5. Wang, Q., Ding, S. L., Li, Y., Royall, J., Feng, D., Lesnar, P., Graddis, N., Naeemi, M., Facer, B., Ho, A., Dolbeare, T., Blanchard, B., Dee, N., Wakeman, W., Hirokawa, K. E., Szafer, A., Sunkin, S. M., Oh, S. W., Bernard, A., *et al.* The Allen Mouse Brain Common Coordinate Framework: A 3D Reference Atlas. *Cell* **181,** 936-953.e20 (2020).

6. Zhuang, J., Ng, L., Williams, D., Valley, M., Li, Y., Garrett, M. & Waters, J. An extended retinotopic map of mouse cortex. *Elife* **6,** 1–29 (2017).

7. Jun, J. J., Steinmetz, N. A., Siegle, J. H., Denman, D. J., Bauza, M., Barbarits, B., Lee, A. K., Anastassiou, C. A., Andrei, A., Aydın, Ç., Barbic, M., Blanche, T. J., Bonin, V., Couto, J. J., Dutta, B., Gratiy, S. L., Gutnisky, D. A., Häusser, M., Karsh, B., *et al.* Fully integrated silicon probes for high-density recording of neural activity. *Nature* **in press,** 232–236 (2017).

8. Rossant, C., Kadir, S. N., Goodman, D. F. M., Schulman, J., Hunter, M. L. D., Saleem, A. B., Grosmark, A., Belluscio, M., Denfield, G. H., Ecker, A. S., Tolias, A. S., Solomon, S., Buzsáki, G., Carandini, M. & Harris, K. D. Spike sorting for large, dense electrode arrays. *Nat. Neurosci.* **19,** 634–641 (2016).

9. Siegle, J. H., López, A. C., Patel, Y. A., Abramov, K., Ohayon, S., Voigts, J., Black, C., Voigts, J., Buccino, A. P., Elle, M., Ciliberti, D., Kloosterman, F., Siegle, J. H., López, A. C., Patel, Y. A., Abramov, K., Ohayon, S. & Voigts, J. Open Ephys: An open-source, plugin-based platform for multichannel electrophysiology. *J. Neural Eng.* **14,** (2017).

10. Deligkaris, K., Bullmann, T. & Frey, U. Extracellularly recorded somatic and neuritic signal shapes and classification algorithms for high-density microelectrode array electrophysiology. *Front. Neurosci.* **10,** 1–11 (2016).

11. Hill, D. N., Mehta, S. B. & Kleinfeld, D. Quality metrics to accompany spike sorting of extracellular signals. *J. Neurosci.* **31,** 8699–8705 (2011).

12. Yamin, H. G., Stern, E. A. & Cohen, D. Parallel processing of environmental recognition and locomotion in the mouse striatum. *J. Neurosci.* **33,** 473–84 (2013).

13. Schmitzer-Torbert, N. C. & Redish, A. D. Task-dependent encoding of space and events by striatal neurons is dependent on neural subtype. *Neuroscience* **153,** 349–360 (2008).

14. Hunnicutt, B. J., Jongbloets, B. C., Birdsong, W. T., Gertz, K. J., Zhong, H. & Mao, T. A comprehensive excitatory input map of the striatum reveals novel functional organization. *Elife* **5,** 1–32 (2016).

15. Hintiryan, H., Foster, N. N., Bowman, I., Bay, M., Song, M. Y., Gou, L., Yamashita, S., Bienkowski, M. S., Zingg, B., Zhu, M., Yang, X. W., Shih, J. C., Toga, A. W. & Dong, H.-W. The mouse cortico-striatal projectome. *Nat. Neurosci.* **19,** 1100–1114 (2016).

16. Oh, S. W., Harris, J. a, Ng, L., Winslow, B., Cain, N., Mihalas, S., Wang, Q., Lau, C., Kuan, L., Henry, A. M., Mortrud, M. T., Ouellette, B., Nguyen, T. N., Sorensen, S. a, Slaughterbeck, C. R., Wakeman, W., Li, Y., Feng, D., Ho, A., *et al.* A mesoscale connectome of the mouse brain. *Nature* **508,** 207–14 (2014).